*22nd December 2025*

# Fault migration and basin evolution during complex rifting: examples from the western North Gulf of Evia, Greece

James Wood[1], Rebecca E. Bell[1], Alexander C. Whittaker[1], Saoirse M. Coveney[1], Frank Chanier[2], Fabien Caroir[3], Haralambos D. Kranis[4], Athanassios Ganas[5]

[1] Department of Earth Science & Engineering, Imperial College London, London, UK

[2] Laboratoire d'Océanologie et de Géosciences, Univ. Lille, CNRS, Univ. Littoral Côte d'Opale, Lille, France

[3] Institut des Sciences de la Terre de Paris, Sorbonne Université, CNRS-INSU, Paris, France

[4] Department of Dynamic, Tectonic & Applied Geology, National and Kapodistrian University of Athens, Athens, Greece

[5] Institute of Geodynamics, National Observatory of Athens, Athens, Greece

*Corresponding author:* James Wood (james.wood18@imperial.ac.uk)

## Acknowledgements

This work received funding as part of the TALENTS doctoral network through the European Union's HORIZON-MSCA-2022-DN-01 research and innovation program under grant agreement No. 101119486 (https://www.talents-dn.eu). JW, AW, RB, HK, and AG are beneficiaries of this grant. SC is funded by NERC grant NE/S007415/1 (Science and Solutions for a Changing Planet DTN). We are grateful to SLB for the provision of Petrel (Version 2024.4.0) for use in this project.

# Abstract

Understanding dynamic processes of faulting and basin evolution across timescales in complex rift settings remains a key challenge in active continental tectonics. This is in part due to a limited number of young rift systems with well constrained, high-resolution age models derived from subsurface datasets. We aim to address this challenge and advance our understanding of time-dependent geodynamic rift processes by developing a late-Quaternary, syn-kinematic age model for the Western Basin of the North Gulf of Evia, Central Greece. In contrast to the nearby Gulf of Corinth, extension here is complicated by rotational and strike-slip influence from the westward-propagating North Anatolian Fault. Seismic stratigraphic principles are used to identify three key horizons based on reflection termination relationships with ages of ~12 ka, ~130 ka and ~325 ka assigned through a sequence stratigraphic model on deltaic clinoform packages. The age model is applied alongside a network of offshore faults to determine the major structures, depocenters and evolutionary history of the rift. We resolve the major controlling faults to be the Kalypso Fault (~4 mm/yr slip) at the southern margin of the basin and the Central Graben (~1-2 mm/yr slip) along the axis of the gulf. We show that the Kalypso Fault is linked to the onshore Coastal Fault System following a migration event with evolving strike from the onshore Arkitsa Fault. The timing of this event is constrained to ~325 ka based on hanging wall sediment thickening relationships and the Kalypso Fault displays immediate, rapid lateral growth and throw accumulation after initiation. Improved constraints on the timing and evolutionary behaviour of young normal fault systems such as this show that fault migration and activation in complex rift settings can occur over timescales less than $10^5$ years.

# Graphical Abstract

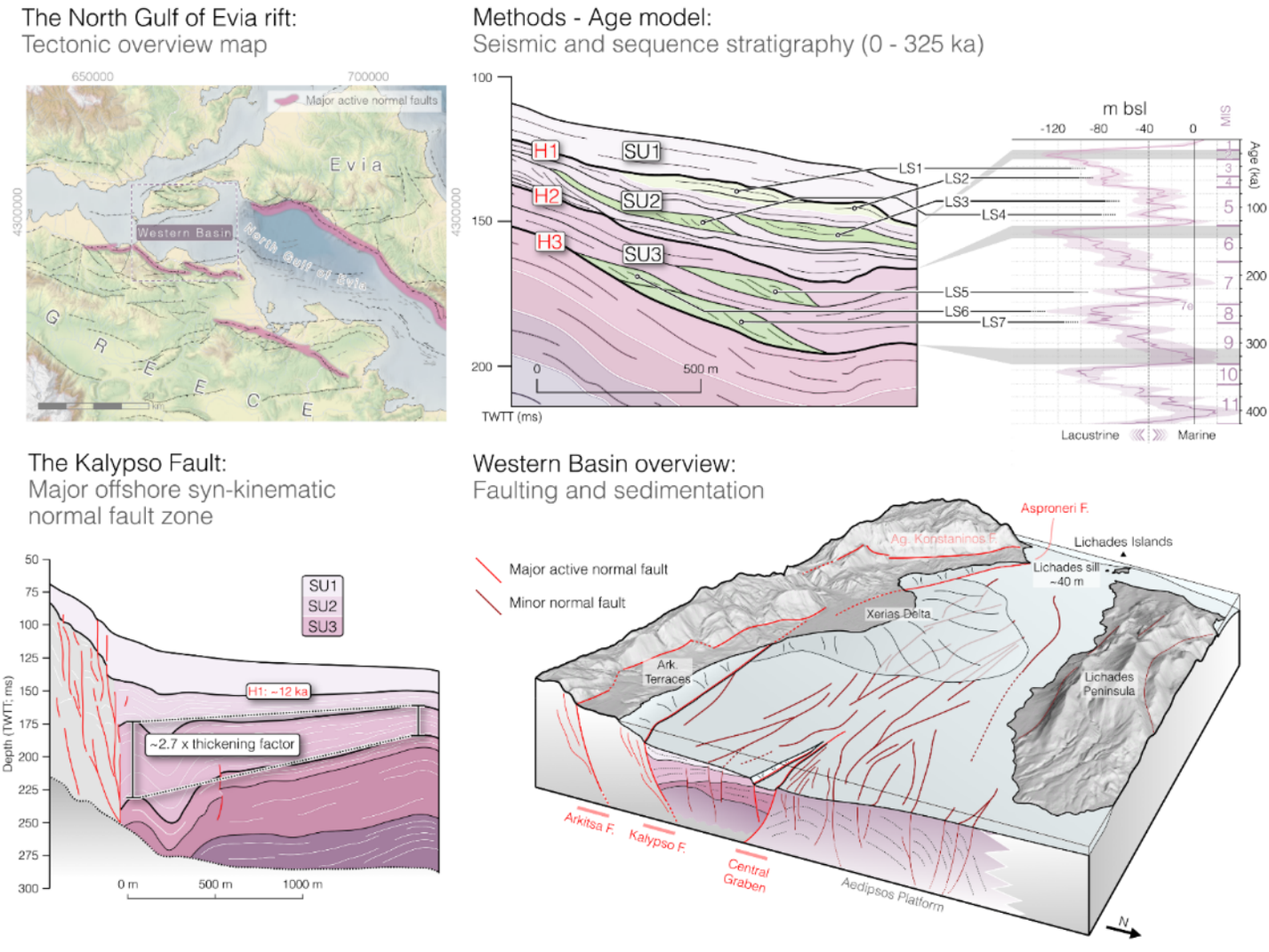


# 1. Introduction

Understanding the timing of fault initiation and strain localisation in rifts is of key importance for constraining models of continental extension, syn-tectonic basin evolution, and seismic hazard. However, as young continental rifts are some of the most dynamic tectonic systems on Earth (Brune et al., 2023), any detailed reconstruction of the timing of fault initiation, linkage and migration typically demands a high-resolution age model of syn-kinematic stratigraphy (Gawthorpe and Leeder, 2000). However, available age models in active rifts at

sufficient detail to allow fault slip rates and timings of initiation, linkage and migration to be resolved over high-resolution timescales ($10^3$-$10^4$ years) are sparse.

Rifting is rarely a simple process, as fault systems may develop oblique to extensional strain (e.g., Agostini et al., 2009; Brune, 2014; Jourdon et al., 2020), basement inheritance can influence fault system growth and migration (e.g., Brune et al., 2017; Molnar et al., 2017; Phillips et al., 2019), and crustal block rotation can introduce evolving principal stress orientations in the rift (e.g., Bradley et al., 2013; Zwaan et al., 2020; Zwaan and Schreurs, 2020). Temporal and spatial reconstructions of normal fault dynamics from natural examples in complex and rotational rift settings are extremely limited at present and high-resolution age models are required to unlock detailed study into the geodynamics and mechanics of these systems.

Syn-rift sedimentation in evolving basins, typically imaged at depth with seismic reflection data, provides an integrated, but often complex, record of both tectonic and environmental forcing (Gawthorpe and Leeder, 2000). However, where tectonic signals can be isolated effectively, for instance through the reconstruction of prevailing environmental conditions (e.g., base level), analysis of syn-rift stratigraphy can provide powerful, quantitative insights into slip rates and evolution of normal fault systems (e.g., Bell et al., 2009, 2008; Feng et al., 2016; Gawthorpe et al., 2018; Nixon et al., 2024, 2016).

The Gulf of Corinth, Greece represents one of the only marine continental rift systems with a high-resolution age model thanks to extensive high-resolution seismic reflection datasets (see Nixon et al., 2016) and deep offshore drilling (McNeill et al., 2019; Nixon et al., 2024). The age models developed for the Gulf of Corinth generated a framework for the rift to become one of the foremost natural laboratories for the detailed study of normal faulting processes (e.g., Bell et al., 2017; de Gelder et al., 2019; Fernández-Blanco et al., 2019; Mildon et al., 2024) and basin sedimentation (e.g., Gawthorpe et al., 2017; McNeill et al., 2019; Watkins et

al., 2018). However, the geodynamics of rifting in the Gulf of Corinth are relatively simple. Extension is orthogonal to the rift system, the evolution of the rift is controlled by the basinward migration of sub-parallel normal fault systems, and strike-slip associations are limited (Ford et al., 2017; Gawthorpe et al., 2018; Leeder et al., 2008; Nixon et al., 2024, 2016).

The North Gulf of Evia, located ~100 km north of the Gulf of Corinth, provides an example of a contrasting style of complex rifting to Corinth and represents a key extensional system in Central Greece (Figure 1). Here, rifting is complicated by marked rotational and strike-slip influence from the westward-propagating North Anatolian Fault (Caroir et al., 2024; Ganas et al., 2016; Hatzfeld et al., 1999; Sboras et al., 2025) and the complexity of the system is exaggerated by oblique fault systems (Kranis et al., 2001; Palyvos et al., 2006), asymmetric normal fault geometries (Goldsworthy et al., 2002), and the reactivation of inherited Alpine structures (Chanier et al., 2024; Kranis, 2007). The North Gulf of Evia therefore provides an excellent opportunity to advance our understanding of rifting and normal faulting processes when coupled with geodynamic or lithospheric complexity.

In this study we utilise a high-density, high-resolution 2D seismic reflection dataset to develop a consistent seismic and sequence stratigraphic age model for late-Quaternary syn-tectonic sedimentation (0 – ~325 ka) of the western North Gulf of Evia (Figure 2). A new offshore network of normal faults is mapped, and we apply the age model to reconstruct a detailed, late-Quaternary history of fault slip and basin development in the Western Basin of the Gulf. Normal fault migration processes are examined in detail in relation to the continental rotation in the Western Basin and in doing so, the work sheds new detailed insight into the temporal evolution of complex rift systems over timescales of $10^4$-$10^5$ years.

# 2. Geological Background

## 2.1 Tectonic setting

The North Gulf of Evia is one of a series of young, ~E-W striking rift systems spanning the continental block of mainland Greece (Figure 1; Goldsworthy et al., 2002; Papanikolaou, 2021; Roberts and Ganas, 2000; Roberts and Jackson, 1991). Extension is thought to be controlled by the rollback of a shallowly subducting African Plate (Jolivet et al., 2013) with regional influence from the westward-propagation of the North Anatolian Fault and westward extrusion of the Anatolian Plate (Figure 1; Caroir et al., 2024; Goldsworthy et al., 2002; Hatzfeld et al., 1999; Sboras et al., 2025). This influence is responsible for 5-8°/Myr rotation of the continental block between the gulfs of Evia and Corinth (Bradley et al., 2013; Briole et al., 2021; Chousianitis et al., 2024) and the extensive strike-slip associations in the North Gulf of Evia (Figure 2; Caroir et al., 2024; Ganas et al., 2016; Kranis et al., 2001; Palyvos et al., 2006).

Although modern geodetic opening rates of 2.9-3.7 mm/yr (Sboras et al., 2025) are ~4 times slower than in the neighbouring Corinth Rift (Briole et al., 2021; Chousianitis et al., 2024), large, damaging earthquakes are known to have occurred around the North Gulf of Evia including the 1894 Atalanti events (Mw 6.4-6.9; Ganas et al., 1998; Pantosti et al., 2004) and the unattributed tsunami-generating earthquake of 426 BCE (Freitag and Reicherter, 2019).

The modern tectonic geometry of the North Gulf of Evia is divided into the Western, Central and Eastern Basins based on bathymetric and subsurface character (Sakellariou et al., 2007; Fig. 1b). Here we consider the Western Basin, a sub-basin at the margin of the gulf between the Coastal Fault System and the Lichades Peninsula (Figure 2b) with the highest extensional strain accommodation in the gulf (~3.7 mm/yr; Sboras et al., 2025). The Coastal Faults span from Arkitsa to beyond Kammena (*or Kamena*) Vourla (~30 km) as a segmented but linked

onshore active normal fault array with a late-Quaternary footwall-component uplift rate of 0.2-0.6 mm/yr (Whittaker and Walker, 2015). The fault system is typically considered the most active structure of the modern rift (Goldsworthy et al., 2002; Roberts and Jackson, 1991). The segments of the Coastal Faults vary in orientation and dip but ubiquitously display north-oriented slip vectors (Figure 2b; Kranis 2007).

Despite evidence for Holocene slip on the Coastal Faults (Kranis, 2007), the geomorphology of the hanging wall land strip shows evidence for rapid uplift (c.f. Wood et al., 2025). This includes the uplifted marine terraces at Arkitsa (Figure 2b) and Holocene coastal notches at Kynos (Supplementary Figure S1) which may indicate the dominant normal faults have migrated offshore (Papanastassiou et al., 2014; Pirazzoli et al., 1999).

## 2.2 Pleistocene palaeoenvironment

Sedimentation in basins is a record of prevailing relative sea, lake or river level (Vail et al., 1977). Isolating tectonic signals from the sedimentary packages imaged in seismic reflection data demands a comprehensive reconstruction of environmental conditions (e.g., base level, sill level and sedimentary environment).

The North Gulf of Evia is a semi-enclosed basin with distinct marine, lacustrine and brackish intervals over the late-Quaternary controlled by sills in the Oreoi and Lichades Straits at 40-45 m bsl (below mean sea level; Figure 2b). Intervals where eustatic sea level is below sill level are interpreted as lacustrine or brackish in the Gulf and eustatic highstands above ~40 m bsl are considered marine. It is probable that most of the Pleistocene lakes of the North Gulf of Evia were restricted to the deepest part of the basin where many submerged terraces have been mapped in vintage seismic datasets (Van Andel and Perissoratis, 2006).

The sill level at Lichades (Figure 2b) has likely varied over time. InSAR-derived ground motion data indicates ~1 mm/yr of uplift over 2019-2023 on the island of Lichades and the coastal land strip at Kammena Vourla (Wood et al., 2025). The shallowing of the sill has

been independently inferred through analysis of Pleistocene microfossil assemblages (Drinia et al., 2014).

The main fluvial drainage of the rift system, the Sperchios River (Figure 2a) reflects a closed sedimentary system throughout the Holocene with all transported sediment deposited in its delta at the Maliakos Gulf (Pechlivanidou et al., 2018). During lowstand conditions, the river likely drained through the Oreoi Channel (Figure 2a), although it is possible that drainage fluctuated to the endorheic North Gulf of Evia Pleistocene lakes where deltaic packages are resolved in seismic reflection data (Caroir et al., 2024; Van Andel and Perissoratis, 2006). The Western Basin therefore likely alternated between a sedimentary sink and fluvial transfer zone depending on prevailing base level and rate of accommodation generation, representing a key contrast to the Gulf of Corinth where basin geometry is largely stable across lacustrine and marine intervals (Gawthorpe et al., 2018).

# 3. Data and Methods

## 3.1 Seismic data and stratigraphic age model

Here, a high density, high resolution seismic reflection dataset across the Western Basin is used to explore the sedimentary and tectonic development of the sub-basin in detail (WATER I and II; Chanier and Gaullier, 2017; Chanier and Watremez, 2021; Figure 2b, Supplementary Figure S5). The WATER surveys acquired ~1800 km of single channel sparker (50-300 J) seismic profiles across the North Gulf of Evia, Oreoi Channel and Skopelos Basin. The subset of 41 profiles used in this study are ca. 350 ms at maximum interpretable depth (~260 – 320 m) and data is typically interpreted to the first seabed multiple which obscures the signal below. Seismic velocities are modelled as 1500 m/s for seawater and 1800 m/s for depth conversions consistent with Caroir et al. (2024).

171 The WATER dataset has been studied previously to determine the regional structural
172 anatomy of the North Gulf of Evia and show the influence of strike-slip deformation at the
173 western termination of the North Anatolian Fault (Caroir et al., 2024). However, no pre-
174 Holocene age correlations have been made for the sedimentary stratigraphy in the offshore
175 North Gulf of Evia to date.

176 In this study, key seismic horizons (H1-H3) are identified in the dataset based on seismic
177 terminations including onlap relationships and erosive truncation (Catuneanu, 2002; Vail et
178 al., 1977). Between these horizons, seismic units (SU1-3) are defined and each unit is
179 characterised based on seismic attributes and geological significance, consistent with seismic
180 facies principles (Vail et al., 1977; Xu and Haq, 2022). Three-dimensional surfaces are
181 produced from the key seismic horizons to analyse spatial variability of sediment package
182 thickness across the gulf (Supplementary Figure S3) with isopachs for each SU calculated as
183 the difference between two surfaces.

184 Age estimates for the seismic horizons and units are derived from sequence stratigraphic
185 principles as unconformity-bounded sediment sequences at the margins of marine and
186 lacustrine systems preserve a record of relative base level change (Catuneanu, 2002; Vail et
187 al., 1977). In clastic systems at basin margins, deltas build up (i.e., aggrade) to prevailing
188 base level before growing outwards (i.e. prograde). When preserved in the geologic record,
189 these packages can be used to infer the sequential timing of local highstand and lowstand
190 periods (Catuneanu, 2002). For late-Quaternary sedimentation, well constrained eustatic sea
191 level curves (e.g., Spratt and Lisiecki, 2016) can be correlated to sequences of clinoforms to
192 generate age models for basin sedimentation (e.g., Bell et al., 2008; Lykousis et al., 2007a).

193 In the south of the Western Basin, a well-developed sequence of submerged clinoform
194 packages is found on seismic lines 107 and 049. These packages are used to establish age
195 estimates for seismic horizons through correlation to the sea level curve of Spratt and Lisiecki

(2016; Figure 3 and 4). Distinct clinoform package rollover points (i.e. topset to foreset transition) are identified in seismic profiles and act as markers of past marine or lacustrine relative base level in the gulf (Catuneanu, 2002). To establish if a clinoform package best correlates to a highstand or lowstand interval, package geometry, apparent base level and stratigraphic sequencing are considered (Catuneanu, 2002; Figure 3a and 3b). Packages are defined as lowstands if they sit stratigraphically above a package with a higher indicated base level or show an exaggerated sigmoidal geometry consistent with decreasing/low accommodation (Figure 3a). Highstand sequences are defined if they build up to higher base level than the underlying stratigraphic package (Figure 3b). Ages are provided with reference to Marine Isotope Stages (MIS) and numeric values are assigned from the sea level stack of Spratt and Lisiecki (2016).

Sill level is marked on base level diagrams at 40 m bsl and at a level consistent with an uplifting sill at 0.1 mm/yr (i.e. 10 year period of 1 mm/yr uplift every 100 years; Wood et al., 2025). Base levels below sill level are considered lacustrine and above are considered marine.

## 3.2 Identification and classification of normal faults

Offshore faults are identified in seismic reflection profiles and mapped across lines to generate three-dimensional geometries. Structures are classified on the most recent key seismic horizon (H1-H3) they offset, providing an estimate for most recent activity. Fault throw is measured as the vertical offset of the key dated seismic horizons defined in the age model across each structure and represents the maximum observable throw on each fault over the given time interval. Throw rates are converted to slip rates with an assumed fault dip of 60-70°, consistent with measured fault planes on the Arkitsa Fault (Kranis, 2007). The full fault database is summarised in more detail in the supplementary material (Figure S4; Table S1 and S2).

Geological field work was conducted in April and October 2025 and included corroborating previous works, refining onshore fault maps (Figure 2) and documenting evidence for onshore uplift and young normal faulting within syn-rift stratigraphy (Supplementary Figure S1).

# 4. Results

## 4.1 Seismic stratigraphy

Three major stratigraphic horizons are identified based on the observation of erosional truncation, onlap terminations and significant changes in seismic character (H1, H2 and H3;). These surfaces can be seen on the seismic profiles of Figure 3c and 4 and their character is summarised in Figure 5.

Both H1 and H2 are highly erosive with overlying sediments commonly onlapping these surfaces (Figure 3 and 4). These horizons each represent a depositional hiatus in the gulf, representing extended periods of subaerial erosion when the North Gulf of Evia lake was restricted to the deep Central basin (Van Andel and Perissoratis, 2006).

A significant change in seismic facies occurs across surface H3 (Figure 5). Younger, overlying sediments are dominated by high amplitude reflectors and abundant clinoforms while below H3, reflections are dominantly low amplitude punctuated by thin, high amplitude packages (Figure 5 and 6). In places, overlying reflections onlap H3 (Figure 6b).

H1 to H3 bound three seismic units defined in Figure 4 (SU1-3). SU1 is found between the seabed and H1. It is dominated by acoustically transparent fan deposits with a thin, high amplitude drape elsewhere. SU1 is equivalent to the Upper Sequence of Caroir et al. (2024) which is considered to represent Holocene sedimentation in that study. Shallow coring of this seismic unit in the Central Basin has confirmed the Holocene age of these sediments (Drinia

et al., 2014; Sakellariou et al., 2007). The fan deposits that dominate the Western Basin are derived from the Xerias River (Figure 2b; Van Andel and Perissoratis, 2006). The erosive surface H1 therefore formed during the Last Glacial Maximum (MIS 2, ~12 ka).

SU2 is found between H1 and H2. It is highly variable in thickness, owing to erosive surfaces at both the base (H2) and top (H1) of the unit and is characterised by abundant clinoforms and onlapping reflectors (Figure 5 and 6). The reflections in the unit are typically high amplitude which, based on seismic reflections and age correlations in the Gulf of Corinth (e.g., Bell et al., 2008; Nixon et al., 2016), implies highstand conditions dominate sedimentation during this time.

SU3, between H2 and H3, is similarly characterised by high amplitude reflections but tends to be more laterally continuous and lower frequency than SU2 with fewer clinoforms (Figure 4). The unit, in deeper basin settings transitions from high amplitude to low amplitude while in marginal depositional settings is nearly exclusively high amplitude with abundant internal and external onlap relationships (Figure 6). SU3 unit is interpreted to represent highstand sedimentation in a marginal sub-basin prior to subaerial exposure and the formation of H2.

## 4.2 Sequence stratigraphy

Sequence stratigraphy of deltaic clinoform packages in Figure 2 and 3 is used to attribute ages to the seismic stratigraphy outlined above through correlation to expected base level in the gulf. Within the sedimentary succession spanning H1 to H3 shown in Figure 2c and 2d, nine distinct packages are identified. Based on the ordering of apparent relative base levels and sequence geometries outlined in the schematic diagrams of Figure 2a and 2b, each package is classified as a relative lowstand or highstand.

Seven lowstand indicators are interpreted between 98 and 135 m bsl (LS1-LS7). These packages have cross-sectional widths of 200-600 m with heights of ~10-20 ms (~9-18 m). LS1 and LS2 sit directly below H1 and indicate similar relative base levels of 98 and 109 m

268 respectively. As H1 very likely represents the base-Holocene surface (see section 4.1), these
269 clinoforms must have developed during moderately high lake level or brackish deposition in
270 MIS 3 at a base level between sill level and ~-80 m bsl (Figure 3d). Lake levels in both MIS
271 2 and MIS 4 were restricted to the Central Basin (Figure 1b; Van Andel and Perissoratis,
272 2006) so deltaic clinoforms are unlikely to have developed in this part of the Western Basin
273 during those intervals.

274 HS1, LS3, HS2 and LS4 follow in the stratigraphic sequence and compose the remaining
275 strata of SU2. HS1 and HS2 are interpreted as highstands as both aggradation of >40 m and
276 retreat towards the basin margin of ~1.2 km are resolved for these packages (see comparison
277 to Figure 3b). The rollover of HS1 is not imaged here so the apparent relative base level of
278 ~70 m bsl is considered a minimum possible value. LS3 (~118 m bsl) sits stratigraphically
279 above HS1 while LS4 (~114 m bsl) sits between HS1 and HS2 with the morphologies and
280 stratigraphic relationships of the two lowstand patterns indicative of a forced regression (see
281 comparison to Figure 2a). The downdip extension of the HS1 package bifurcates above and
282 below LS3 while the up-dip extent of this unit drapes HS2. Based on this sequencing, these
283 four packages are attributed to MIS 5 with HS2 being MIS 5e and the thin sediment drape
284 above this of HS1 likely being an amalgamation of MIS 5c and 5a. Significant local
285 subsidence between MIS 5e and 5c is required to allow this drape at a sea level that is
286 expected to be ~25 m lower than the extreme highstand of MIS 5e (Figure 3d). Based on
287 sequencing relationships to these highstands, LS3 is attributed to MIS 5b and LS4 assigned to
288 MIS 5d (Figure 3d).

289 Horizon H3 is located below this and, given its character as a strongly erosive surface, best
290 represents late-MIS6 when the Western Basin likely saw an extended period of subaerial
291 exposure following significant base level fall. Immediately below this surface is a package of
292 consistent deposition without a preserved associated clinoform package (Figure 3c). LS5
293 (~126 m bsl) is a laterally restricted clinoform package with an indicated relative base level

far below the underlying unit. It is therefore considered a lowstand interval (Figure 3a). LS6 (~125m bsl) is a narrow (~200m) clinoform set that builds up above the underlying package (LS7; ~135 m bsl). However, it does not build up above horizon H3 and, given aggradation from LS7 to LS6 is only ~10 m, both are considered lowstand packages. The stratigraphic positioning of LS5 best fits a moderate lowstand during MIS 7 (MIS 7d) with overlying sediment representing subsequent periods of higher sea level (i.e., MIS 7c-a). Finally, the two closely related packages of LS6 and LS7 sit below a further interval of highstand sedimentation (MIS 7e) and are best correlated to MIS 8.

Surface H3 marks the base of the interpreted clinoform packages in Figure 3c and 3d and, given its nature as a cap to a high amplitude package marking a significant change in basin sedimentation, is attributed to MIS 9e (Figure 3d). Correlation below H3 is uncertain due to poor imaging in the seismic reflection dataset across the basin.

Figure 4a shows a well-developed sequence of clinoforms on an intersecting seismic profile to Figure 3c (Figure 4b). All packages marked in Figure 4a are characterized as lowstand intervals based on comparison to expected geometries (Figure 3a) with two packages developed on the southeastern margin and four developed on the northwestern margin of a small paleo-bathymetric depression. Stratigraphic sequencing here is comparable to Figure 3c and all lowstand packages from Figure 3c are represented in this adjacent line, except LS2 which is not locally developed. Indicated base levels in Figure 3a are within 10% of counterparts in Figure 3c for each resolved lowstand package except LS1 which has an indicated depth of 17 m lower. This may imply heightened tectonic subsidence has occurred at the southeastern end of this profile.

Based on this sequence stratigraphic model across both Figure 3 and 4, age estimates of H1-3 and SU1-3 are derived and attributed to the seismic stratigraphic architecture of Figure 5. In

short, H1 represents MIS 2 (~12 ka), H2 represents late-MIS 6 (~130 ka) and H3 represents MIS 9e (~325 ka).

Key to the utility of the age model is that it can be mapped consistently across the Western Basin and wider North Gulf of Evia. Figure 6 shows interpreted seismic profiles that span the axial length of the Western Basin (Figure 6a) and cross the width of the study area (Figure 6b) with the age model of Figure 5 applied. The erosive nature of H1 and H2 and the acoustic transparency of SU1 are well highlighted in Figure 5a and the onlapping relationships of H1-3 are highlighted in the south of Figure 6b. The marked change in seismic expression beneath horizon H3 is evident in across both profiles with a shift from high amplitude reflections dominating above to low amplitude reflections below. Where apparent in Figure 6a, clinoforms are restricted to SU2 and SU3 with indicated paleo-flow directions to the west. A substantial (~2 km wide) clinoform package attributed to MIS 5e on line 229 also indicates flow to the west. These flow directions are opposed to expected drainage to the southeast based on modern depocenters (Figure 2).

## 4.3 Normal fault network

Application of the age model to develop a full tectonic evolutionary history of the Western Basin demands a comprehensive map of offshore normal faults. Figure 7a and 7b show the mapped offshore fault network from this study. 47 offshore fault segments are mapped with lengths of 0.5 km to 12 km (see Supplementary Table S1 and S2). The structural fabric of the offshore rift is characterised by dominantly E-W striking normal faults, following the axis of the gulf (Figure 7). The density of sub-parallel normal faults across the width of the gulf increases from west to east as 3 to 4 structures span the basin near Neochori and 16 faults are mapped across the basin in the east (Figure 7a).

The base-Holocene surface (i.e. depth to H1 erosive surface) shown in Figure 7a and 7b provides a clearer indication of Pleistocene depocenters of the basin than modern bathymetry

as the thick fan deposits from the Xerias River (Figure 2b) are stripped away. This surface allows primary depocenter-controlling structures to be identified.

The fault network in Figure 7a is classified on most recent evident fault slip derived from the youngest mapped horizon (H1-3) that they offset. Active faults (i.e. structures that offset H1 or the seabed) are depicted in red while faults that do not offset H1, H2 or H3 are considered least active (grey). Figure 7b classifies each structure on the maximum resolved throw rate in this study with separate rates calculated between each age-attributed horizon (Figure 5). Only three faults exhibit throw rates of >0.75 mm/yr (F01, F08 and F10) with the highest throw rate in the basin of ~3.75 mm/yr during the Holocene resolved for F01. Across all normal faults, a median throw rate of 0.2 mm/yr is resolved.

The southeast of the Western Basin appears to be controlled by a single, east-northeast striking (~260°) major normal fault zone (F01), here named the Kalypso Fault (from the homonymous settlement west of Arkitsa; Figure 7a). At the eastern tip of the fault, spacing to the onshore Arkitsa Fault segment is ~4 km with negligible spacing between the structures in the west, particularly when the onshore continuation of the fault is considered (Figure 7a). A potentially active normal fault had previously been inferred here based on the uplifted marine terraces between the Arkitsa Fault and the modern coastline (Cundy et al., 2010; Papanastassiou et al., 2014) and the fault is mapped as WB4 in the regional structural analysis of Caroir et al. (2024). We find the onshore continuation at the western extent of the Kalypso Fault to follow a topographic escarpment (Figure 7) where fault breccia with syn-rift clasts and fault surfaces (79/025; dip/azimuth) are found (Supplementary Figure S1a).

The Central Graben, consisting of a major south dipping and north dipping normal fault (F10 and F08), is located along the axis of the gulf in the east of the study area (Figure 7). The graben opens significantly to the east with a fault spacing of 200 m at the western tip of the graben and > 2.5 km in the east (Figure 7a). The main faults of the graben appear to trend

368 further to the east to bound the deep Central Basin, suggesting the faults are a significant
369 modern bathymetric control in the gulf (c.f., Caroir et al., 2024). Slip is considerable on these
370 structures with Holocene throw rates of 0.9 mm/yr on the south dipping fault and 1.7 mm/yr
371 on the north dipping fault (Figure 7b).

372 The Asproneri Fault (F43) in the southwest generates a significant bathymetric escarpment
373 and appears to be a major control on accommodation generation in this area (Figure 6b and
374 7a). This structure is likely responsible for uplifted terraces in the hanging wall of the onshore
375 Agios Konstantinos Fault (Figure 2b; Supplementary Figure S1c). However, slip rates and
376 along-strike variation for this structure are poorly resolved due to the low density of seismic
377 profiles here (Figure 2b).

## 378 4.4 Syn-kinematic sedimentation

379 Integrating the sedimentary age model with the normal fault network in Figure 6 constructs a
380 picture of how major depocenters in the Western Basin have changed over time in response
381 to tectonic and environmental forcing. The syn-tectonic thickening of sediment packages into
382 the hanging wall of normal faults also provides an indication of timing, and rates, of fault
383 activity as hanging wall subsidence generates heightened accommodation space (e.g.,
384 Coveney et al., 2025; Gawthorpe and Leeder, 2000; Jackson et al., 2017). Figure 8 shows
385 sediment thickness isopachs of the three seismic units defined in Figure 5 (SU1-3) with the
386 thickening direction of each unit SU1-3 indicating the major structural controls on syn-rift
387 sedimentation at the time.

388 Figure 8a depicts a Holocene-only (SU1) isopach. In the west, sedimentation is dominated by
389 the ~50 m thick deposits of the Xerias Fan, while in the east, Holocene sedimentation is
390 thickest between the Kalypso Fault and a south-dipping series of faults ~3 km to the north
391 (F02, F03, F46 – Figure 7). Elsewhere in the Western Basin, a thin drape of SU1 caps the
392 underlying succession.

Figure 8b shows the thickness of SU2. This isopach also shows thickening towards the south and the Kalypso Fault to a maximum thickness of ~30 m. Yet, preserved sediment thickness of SU2 shows high variability due to an apparently wider spatial distribution of active faulting during this time and erosion from the overlying H1 unconformity.

Figure 8c also shows significant thickening of SU3 to the south across both the east, towards the Kalypso Fault, and west, towards the Asproneri Fault. Post-depositional faulting and subaerial erosion during MIS 6 (H2) and MIS2 (H1) results in similarly high variability in this isopach to Figure 8b.

Figure 8d shows a further isopach constructed from a pre-325 ka sediment package that is only correlated across the deeper southeast of the study area due to poor imaging elsewhere. In contrast to the overlying units, this package shows a thickening trend towards the north, showing an inverted polarity of thickening. This implies that the major control on accommodation generation in the depocenter during this interval was likely the south-dipping fault of the Central Graben (Figure 8d and 9).

These sediment thickening trends are also depicted in profile in Figure 9. Here, SU1-3 show significant syn-tectonic thickening into the immediate hanging wall of the Kalypso Fault. SU3, for example thickens from 20 m to 54 m over 1.5 km towards the fault zone (Figure 9b). Packages below SU3, such as the pre-325 ka package mapped in the isopach of Figure 8d, maintain constant thickness into the Kalypso fault plane and instead thicken significantly towards the Central Graben in the north (Figure 9a and 9b). This provides evidence that the Kalypso Fault likely initiated to become the dominant syn-sedimentary control on the Western Basin immediately prior to the deposition of SU3 (~325 ka).

Figure 9a also directly images the fault zone of the Kalypso Fault. From the offset of the ~12 ka surface across the Kalypso Fault (~45 m) in this profile, a maximum Holocene throw rate of ~3.75 mm/yr is resolved (Figure 9b). Considering a long-term uplift to subsidence ratio of

1:2-3, consistent with normal faults in the Gulf of Corinth (e.g., Armijo et al., 1996; McNeill et al., 2005; Nixon et al., 2024), the Kalypso Fault is likely responsible for ~0.9-1.3 mm/yr footwall uplift. This is comparable to the estimated 1-1.5 mm/yr uplift rates derived for the Arkitsa marine terraces in the immediate footwall of the Kalypso Fault, based on $^{14}C$ dating of shelly fauna (Papanastassiou et al., 2014).

# 5. Discussion

## 5.1 Pleistocene evolution of the Western Basin

The seismic stratigraphic age model developed in this study (Figure 5) represents the first pre-Holocene correlation proposed for the North Gulf of Evia. The age model is applicable and consistent across the Western Basin (Figure 6) and allows both for the timing of fault activity and the first estimates of Pleistocene slip rates of offshore normal faults in the North Gulf of Evia to be derived (Figure 7). This has allowed several key events in the evolution of the offshore Western Basin to be resolved as presented in the schematic evolutionary block models of Figure 10a-c.

The initiation of the Kalypso Fault at ~325 ka, depicted in Figure 10a, represents a marked change in the major depocenter geometry and structural control in the gulf with older sedimentary units showing thickening towards the axial Central Graben (Figure 8d).

Following this, base level fall and subaerial exposure of the Western Basin resulted in significant erosion (H2) and drainage reorganisation during late-MIS 6 (~130 ka; Figure 10b). A similar significant regression occurred in the gulf during MIS 2, allowing the erosive H2 seismic surface to develop (Figure 5). During these extreme lowstand intervals, the studied area represents a fluvial transfer zone for drainage towards the main sedimentary sink of the rift system in the Central Basin (Figure 10b). The dominant westward paleo-flow direction of clinoform packages in SU1 and SU2 of Figure 6a (opposite to modern drainage)

suggests that drainage reorganisation has been a common occurrence in the Western Basin throughout the late-Pleistocene.

Subsequent flooding of the basin in the Holocene has promoted the rapid progradation of the Xerias Delta, which has dominated Western Basin deposition over the Holocene (Figure 8a, 10c and 10d).

## 5.2 Age model comparison to the Gulf of Corinth

Comparing the age model presented in this study to similarly constructed age models for syn-rift sedimentation in the Gulf of Corinth (e.g., Bell et al., 2008; Lykousis et al., 2007b; Nixon et al., 2016) reveals a number of key similarities and differences between the rifts.

Like the offshore age models for basin sedimentation in the Gulf of Corinth (e.g., Bell et al., 2008; Nixon et al., 2016) our age model is constrained by key seismic horizons representing intervals of rapid environmental (i.e. base level) change. We define three key horizons (H1-3) while seven key horizons are defined in the Gulf of Corinth age model of Nixon et al. (2016), owing to deeper imaging of seismic reflection data there. H1 (~12 ka) and H2 (~130 ka) in our study correlate with the upper two key horizons (H1 and H2) in the Gulf of Corinth (Nixon et al., 2016). Horizon H3 from our study has a proposed age of ~325 ka and is equivalent to H4 (~340 ka) in the model of Nixon et al. (2016) with the small age discrepancy related to the position within the highstand package the horizon is placed.

The efficacy of the seismic age models of Nixon et al. (2016) and others have recently been tested following International Ocean Discovery Program (IODP) drilling in the Gulf of Corinth (McNeill et al., 2019; Nixon et al., 2024). This drilling has allowed the magneto- and bio-stratigraphic dating of Corinth seismic horizons H1 (13 ka), H2 (129 ka) and H4 (335 ka), finding the proposed ages from the existing seismic stratigraphic model to all be within 5 ka (Nixon et al., 2024).

The seismic expression of the units however highlights several differences between the Western Basin of the North Gulf of Evia and the Gulf of Corinth. Seismic units in the deep basin settings in Corinth alternate between thick low amplitude packages, correlated to lowstand lacustrine deposition, and thin high amplitude packages correlated to marine deposition during highstands (Bell et al., 2008; Nixon et al., 2024). In contrast, the late-Pleistocene seismic units in the North Gulf of Evia are near-universally characterised by high amplitude reflections (Figure 5 and 6). This reflects the exaggerated sensitivity of the North Gulf of Evia to sea level change. This sensitivity is due to a combination of the 40 m Lichades Sill to the Aegean Sea (Figure 2b; 20 m shallower than the Rion Sill to the Gulf of Corinth; McNeill et al., 2019) and the overall shallow bathymetry and palaeo-bathymetry of the Western Basin (<120 m; Figure 7). As a result, sedimentation across much of the sub-basin is restricted to interglacial highstands (e.g., MIS 5, 7 and 9) as lowstand Pleistocene glacial lakes (e.g., MIS 2 and 6) were likely confined to the deep Central Basin (c.f., Van Andel and Perissoratis, 2006). The distinct periods of subaerial exposure of the Western Basin (Figure 10b) are also not widely seen across wide areas in the basins of the Gulf of Corinth (Gawthorpe et al., 2018).

Reliable sedimentation rates are difficult to constrain in the Western Basin due to the strongly developed H1 and H2 erosive surfaces (Figure 5). It is possible to deduce, however, that sedimentation in the Western Basin is markedly slower than in the main depocenters of the Gulf of Corinth. In the well-preserved seismic packages in the south of Figure 9, where erosion appears to be minimal, sedimentation rates of 0.1-0.3 mm/yr are calculated for the thickest sections of SU3 (20-54 m over ~195 kyrs) and 0.1-0.2 mm/yr (10-20 m over ~120 kyrs) for SU2. Despite these rates likely representing maxima in the Western Basin, they are an order of magnitude slower than sedimentation over comparable time intervals in the main depocenters of the Gulf of Corinth of 1-3 mm/yr (McNeill et al., 2019).

## 5.3 Normal fault migration in complex rifts

In the example of the western North Gulf of Evia, the overall structural anatomy of the rift reflects an asymmetric graben with dominant structural control from the onshore Coastal Faults and near-offshore Kalypso Fault (Figure 10d).

A trend of increasing recency of fault activity towards the Central Graben and Kalypso Fault is resolved (Figure 7a). Faults on the northern margin of the basin have not generated significant accommodation, nor do they show significant slip, during the deposition of SU1-3 with the major depocenters found to the south of the Central Graben (Figure 7b and 8). The Kalypso Fault represents the northernmost migration of the fault systems of the southern margin of the rift while migration from north has localised on the Central Graben (Figure 6b). Holocene slip in the Central Graben is significant with ~2 mm/yr slip on the north-dipping structure and ~1 mm/yr slip on the south-dipping fault. The south-dipping fault generated significant hanging wall accommodation prior to ~325 ka (Figure 7d and 8).

Faults on the northern margin of the western basin appear to have migrated to broadly parallel structures (Figure 7a). In contrast, the main migration event on the southern margin from the Arkitsa Fault to Kalypso Fault has occurred across non-parallel faults with evolving strike (Arkitsa = ~280°; Kalypso = ~260°; Figure 10d). This is interpreted to reflect the geodynamic rotational influence on fault migration in the gulf. The western tip of both Arkitsa and Kalypso segments join the Agios Konstantinos Fault at the same point resulting in extremely tight fault spacing in this area (Figure 10d). It appears that this western tip has acted as a rotational axis for this migration event.

The strike of the Kalypso Fault also reflects a comparable extension azimuth to the ~70° strike rupture plane resolved for the 2013 Mw = 5.4 Kallidromon earthquake sequence in the same tectonic system (Ganas et al., 2014). This is consistent with measured strain from

515 geodetic studies which show present extension acts at an azimuth of ~0 - 10° (Briole et al.,
516 2021; Chousianitis et al., 2024; Sboras et al., 2025).

517 Activity on the Kalypso Fault initiated at ~325 ka, as inferred from a reverse in thickening
518 direction at this time towards the structure (Figure 8 and 9). The uplifted marine terrace
519 staircase in the footwall of the structure (Figure 10; Papanastassiou et al., 2014) implies that
520 footwall uplift of the Kalypso Fault has exceeded hanging wall subsidence of the Arkitsa
521 Fault over the late-Pleistocene. To achieve this, the Kalypso Fault has likely undergone fault
522 linkage to the other segments of the Coastal Fault System. This implies that the Arkitsa Fault
523 has seen a marked reduction in slip rate since the initiation of the Kalypso, in agreement with
524 previous work where late-Pleistocene slip on the Arkitsa Fault is reported to be as low as 0.7
525 mm/yr (Walker et al., 2010; Whittaker and Walker, 2015).

526 The Kalypso Fault has a segment length of ~12 km (Figure 7) and a linked length of ~30 km
527 to the Kammena Vourla Fault segment (Figure 2b). Our resolved throw rate of ~3.75 mm/yr
528 corresponds to a slip rate of ~4.0-4.3 mm/yr assuming fault dip of 60-70° and is consistent
529 with the large normal fault (>10 km length) displacement-length scaling relationships of
530 Lathrop et al. (2022) given an initiation age of 325 ka. The Kalypso Fault presents significant
531 regional seismic hazard and is capable of hosting Mw > 6 earthquakes (Wells and
532 Coppersmith, 1994) and given its offshore location, also presents significant tsunami hazard
533 to the North Gulf of Evia. The Kalypso Fault could provide a potential source for the
534 currently unattributed tsunami-forming earthquake of 426 BCE (Freitag and Reicherter,
535 2019).

536 The establishment of the Kalypso Fault to become the dominant structural control on the
537 western rift occurred rapidly with significant throw accumulation and lateral growth
538 occurring within ~325 kyrs. Syn-kinematic thickening in Figure 9 appears to begin
539 immediately above H3 with no marked change in sediment thickening rate in the units above.

This highlights the rapid onset of slip on the Kalypso Fault to become dominant over timescales less than 100 kyrs, likely close to 10 kyrs, and implies that normal fault migration and establishment in young rift systems occur rapidly over these timescales.

Complex geodynamic settings are common in active rift systems (e.g., Brune et al., 2023; Laó-Dávila et al., 2015; Mouslopoulou et al., 2007; Saria et al., 2014; Wallace et al., 2004) and rifts preserved in the geological record (e.g., Duffy et al., 2015; Frizon de Lamotte et al., 2015). Analogue and numerical models are used explore the influence of rotational strain on rift development (e.g., Duclaux et al., 2020; Molnar et al., 2017; Schmid et al., 2022; Zwaan et al., 2020; Zwaan and Schreurs, 2020) yet natural records of normal fault processes in these settings remain underexamined. Processes such as the oblique fault migration and rapid slip accumulation resolved here on the Kalypso Fault are likely not unique to the North Gulf of Evia and occur across many active and failed rift systems. Adding to the quantity of studies with strong temporal constraints in natural, complex rift settings will help to further develop a detailed understanding of how faults and fault systems grow and migrate rapidly and interact in non-simple tectonic regimes. In turn, this will serve to improve the accuracy and applicability of numerical and analogue models of rift processes.

# 6 Conclusions

This study provides a high-resolution record of normal fault migration and basin evolution during complex rifting from the western North Gulf of Evia, Central Greece. Here extension is influenced by continental block rotation and strike-slip deformation from the North Anatolian Fault (Figure 1 and 2) and as such, the rift offers a structural contrast to the nearby orthogonal rifting in the Gulf of Corinth.

In this work:

- A consistent, syn-kinematic, seismic stratigraphic age model for the North Gulf of Evia is defined for the first time, with three key mappable surfaces (H1-3) attributed ages of ~12, ~130 and ~325 ka, based on a base-level correlation to subsurface clinoform packages.
- Major syn-rift depocentres are located along the southern margin of the basin in the hanging wall of the Kalypso Fault (~4 mm/yr slip rate) and additional significant syn-kinematic control from the axial Central Graben (~1 – 2 mm/yr slip) is observed.
- Basinward migration of the active front of normal faulting is observed on both margins of the rift system over the 10-100s kyr timescales resolved in this study. Faults on the northern margin have migrated to sub-parallel structures (e.g., Central Graben) while fault migration on the southern margin has occurred between structures with evolving strike of ~20° (e.g., Kalypso Fault).
- The Kalypso Fault is found to exert dominant structural control on the basin currently. This initiated at ~325 ka following an oblique fault migration event from the onshore Arkitsa Fault. The Kalypso Fault became established rapidly as the dominant fault over timescales of 10s kyrs and is linked to the existing, onshore Coastal Fault System.

This study demonstrates the value of temporal constraints on syn-kinematic sedimentation derived from high-resolution subsurface data to examine rapidly evolving fault and fault system processes in complex settings.

# Data Availability

The fault network produced from this study is available as a .kml file. Uninterpreted seismic profiles presented in this study are available in the Supplementary Materials. Seismic reflection data is available on request.

# References


Agostini, A., Corti, G., Zeoli, A., Mulugeta, G., 2009. Evolution, pattern, and partitioning of deformation during oblique continental rifting: Inferences from lithospheric-scale centrifuge models. Geochemistry, Geophysics, Geosystems 10. https://doi.org/10.1029/2009GC002676

Armijo, R., Meyer, B., King, G.C.P., Rigo, A., Papanastassiou, D., 1996. Quaternary evolution of the Corinth Rift and its implications for the Late Cenozoic evolution of the Aegean. Geophysical Journal International 126, 11–53. https://doi.org/10.1111/j.1365-246X.1996.tb05264.x

Bell, R.E., Duclaux, G., Nixon, C.W., Gawthorpe, R.L., McNeill, L.C., 2017. High-angle, not low-angle, normal faults dominate early rift extension in the Corinth Rift, central Greece. Geology 46, 115–118. https://doi.org/10.1130/G39560.1

Bell, R.E., McNeill, L.C., Bull, J.M., Henstock, T.J., 2008. Evolution of the offshore western Gulf of Corinth. GSA Bulletin 120, 156–178. https://doi.org/10.1130/B26212.1

Bell, R.E., McNeill, L.C., Bull, J.M., Henstock, T.J., Collier, R.E.L., Leeder, M.R., 2009. Fault architecture, basin structure and evolution of the Gulf of Corinth Rift, central Greece. Basin Research 21, 824–855. https://doi.org/10.1111/j.1365-2117.2009.00401.x

Bradley, K.E., Vassilakis, E., Hosa, A., Weiss, B.P., 2013. Segmentation of the Hellenides recorded by Pliocene initiation of clockwise block rotation in Central Greece. Earth and Planetary Science Letters 362, 6–19. https://doi.org/10.1016/j.epsl.2012.11.043

Briole, P., Ganas, A., Elias, P., Dimitrov, D., 2021. The GPS velocity field of the Aegean. New observations, contribution of the earthquakes, crustal blocks model. Geophysical Journal International 226, 468–492. https://doi.org/10.1093/gji/ggab089

Brune, S., 2014. Evolution of stress and fault patterns in oblique rift systems: 3-D numerical lithospheric-scale experiments from rift to breakup. Geochemistry, Geophysics, Geosystems 15, 3392–3415. https://doi.org/10.1002/2014GC005446

Brune, S., Corti, G., Ranalli, G., 2017. Controls of inherited lithospheric heterogeneity on rift linkage: Numerical and analog models of interaction between the Kenyan and Ethiopian rifts across the Turkana depression. Tectonics 36, 1767–1786. https://doi.org/10.1002/2017TC004739

Brune, S., Kolawole, F., Olive, J.-A., Stamps, D.S., Buck, W.R., Buiter, S.J.H., Furman, T., Shillington, D.J., 2023. Geodynamics of continental rift initiation and evolution. Nature Reviews Earth & Environment 4, 235–253. https://doi.org/10.1038/s43017-023-00391-3

Caroir, F., Chanier, F., Gaullier, V., Sakellariou, D., Bailleul, J., Maillard, A., Paquet, F., Watremez, L., Averbuch, O., Graveleau, F., Ferrière, J., 2024. Late Quaternary deformation in the western extension of the North Anatolian Fault (North Evia,

626 Greece): Insights from very high-resolution seismic data (WATER surveys).
627 Tectonophysics 870, 230138–230138. https://doi.org/10.1016/j.tecto.2023.230138
628 Catuneanu, O., 2002. Sequence stratigraphy of clastic systems: concepts, merits, and pitfalls.
629 Journal of African Earth Sciences 35, 1–43. https://doi.org/10.1016/S0899-
630 5362(02)00004-0
631 Chanier, F., Ferrière, J., Averbuch, O., Graveleau, F., Caroir, F., Gaullier, V., Watremez, L.,
632 2024. The Main Pelagonian Detachment (MPD): extensional reactivation of the
633 frontal thrust of the Internal Zones of the Hellenides (Greece). Comptes Rendus.
634 Géoscience 356, 207–229. https://doi.org/10.5802/crgeos.255
635 Chanier, F., Gaullier, V., 2017. WATER cruise, Téthys II R/V, Sismer.
636 https://doi.org/10.17600/17009400
637 Chanier, F., Watremez, L., 2021. WATER 2 cruise, RV Téthys II.
638 https://doi.org/doi.org/10.17600/18001115
639 Chousianitis, K., Sboras, S., Mouslopoulou, V., Chouliaras, G., Hristopulos, D.T., 2024. The
640 Upper Crustal Deformation Field of Greece Inferred From GPS Data and Its
641 Correlation With Earthquake Occurrence. Journal of Geophysical Research: Solid
642 Earth 129, e2023JB028004. https://doi.org/10.1029/2023JB028004
643 Coveney, S.M., Bell, R.E., Wils, K., Lastras, G., Whittaker, A.C., 2025. The Early Evolution
644 of a Young Normal Fault in the Aysén Fjord, Chile. Tectonics 44, e2025TC008835.
645 https://doi.org/10.1029/2025TC008835
646 Cundy, A.B., Gaki-Papanastassiou, K., Papanastassiou, D., Maroukian, H., Frogley, M.R.,
647 Cane, T., 2010. Geological and geomorphological evidence of recent coastal uplift
648 along a major Hellenic normal fault system (the Kamena Vourla fault zone, NW
649 Evoikos Gulf, Greece). Marine Geology 271, 156–164.
650 https://doi.org/10.1016/j.margeo.2010.02.009
651 de Gelder, G., Fernández-Blanco, D., Melnick, D., Duclaux, G., Bell, R.E., Jara-Muñoz, J.,
652 Armijo, R., Lacassin, R., 2019. Lithospheric flexure and rheology determined by
653 climate cycle markers in the Corinth Rift. Sci Rep 9, 4260.
654 https://doi.org/10.1038/s41598-018-36377-1
655 Drinia, H., Antonarakou, A., Anastasakis, G., 2014. Late Quaternary micropalaeontological
656 record of a semi-enclosed marine basin, North Evoikos, central Aegean Sea.
657 Quaternary International 345, 18–31. https://doi.org/10.1016/j.quaint.2014.04.011
658 Duclaux, G., Huismans, R.S., May, D.A., 2020. Rotation, narrowing, and preferential
659 reactivation of brittle structures during oblique rifting. Earth and Planetary Science
660 Letters 531, 115952. https://doi.org/10.1016/j.epsl.2019.115952
661 Duffy, O.B., Bell, R.E., Jackson, C.A.-L., Gawthorpe, R.L., Whipp, P.S., 2015. Fault growth
662 and interactions in a multiphase rift fault network: Horda Platform, Norwegian North
663 Sea. Journal of Structural Geology 80, 99–119.
664 https://doi.org/10.1016/j.jsg.2015.08.015
665 Feng, Y., Jiang, S., Hu, S., Li, S., Lin, C., Xie, X., 2016. Sequence stratigraphy and
666 importance of syndepositional structural slope-break for architecture of Paleogene
667 syn-rift lacustrine strata, Bohai Bay Basin, E. China. Marine and Petroleum Geology
668 69, 183–204. https://doi.org/10.1016/j.marpetgeo.2015.10.013
669 Fernández-Blanco, D., de Gelder, G., Lacassin, R., Armijo, R., 2019. A new crustal fault
670 formed the modern Corinth Rift. Earth-Science Reviews 199, 102919.
671 https://doi.org/10.1016/j.earscirev.2019.102919
672 Ford, M., Hemelsdaël, R., Mancini, M., Palyvos, N., 2017. Rift migration and lateral
673 propagation: evolution of normal faults and sediment-routing systems of the western
674 Corinth rift (Greece). Geological Society, London, Special Publications 439, 131–
675 168. https://doi.org/10.1144/SP439.15
676 Freitag, K., Reicherter, K., 2019. The earthquake and tsunami of 426 BC in Greece:
677 observations by Thucydides and contextual interpretations. Zeitschrift für

678 Geomorphologie, Supplementary Issues 62, 47–62.
679 https://doi.org/10.1127/zfg_suppl/2019/0625
680 Frizon de Lamotte, D., Fourdan, B., Leleu, S., Leparmentier, F., de Clarens, P., 2015. Style of
681 rifting and the stages of Pangea breakup. Tectonics 34, 1009–1029.
682 https://doi.org/10.1002/2014TC003760
683 Galanakis, D., Sboras, S., Sakellariou, D., Pavlides, S., Iordanidou, K., Georgiou, C., Ganas,
684 A., Koukouvelas, I., Kranis, C., Lalechos, S., Rondoyanni, T., Lekkas, E., 2025. The
685 Hellenic DataBase of Active Faults (HeDBAF): a new, national geodatabase of active
686 faults for the broader Greek territory. Presented at the EGU 2025, Copernicus
687 Meetings, Vienna. https://doi.org/10.5194/egusphere-egu25-9230
688 Ganas, A., Karastathis, V., Moshou, A., Valkaniotis, S., Mouzakiotis, E., Papathanassiou, G.,
689 2014. Aftershock relocation and frequency–size distribution, stress inversion and
690 seismotectonic setting of the 7 August 2013 M=5.4 earthquake in Kallidromon
691 Mountain, central Greece. Tectonophysics 617, 101–113.
692 https://doi.org/10.1016/j.tecto.2014.01.022
693 Ganas, A., Mouzakiotis, E., Moshou, A., Karastathis, V., 2016. Left-lateral shear inside the
694 North Gulf of Evia Rift, Central Greece, evidenced by relocated earthquake sequences
695 and moment tensor inversion. Tectonophysics 682, 237–248.
696 https://doi.org/10.1016/j.tecto.2016.05.031
697 Ganas, A., Oikonomou, I.A., Tsimi, C., 2013. NOAfaults: a digital database for active faults
698 in Greece. Bulletin of the Geological Society of Greece 47, 518–530.
699 https://doi.org/10.12681/bgsg.11079
700 Ganas, A., Roberts, G.P., Memou, T., 1998. Segment boundaries, the 1894 ruptures and
701 strain patterns along the Atalanti Fault, Central Greece. Journal of Geodynamics 26,
702 461–486. https://doi.org/10.1016/S0264-3707(97)00066-5
703 Gawthorpe, R.L., Andrews, J.E., Collier, R.E.L., Ford, M., Henstra, G.A., Kranis, H., Leeder,
704 M.R., Muravchik, M., Skourtsos, E., 2017. Building up or out? Disparate sequence
705 architectures along an active rift margin—Corinth rift, Greece. Geology 45, 1111–
706 1114. https://doi.org/10.1130/G39660.1
707 Gawthorpe, R.L., Leeder, M.R., 2000. Tectono-sedimentary evolution of active extensional
708 basins. Basin Research 12, 195–218. https://doi.org/10.1111/j.1365-
709 2117.2000.00121.x
710 Gawthorpe, R.L., Leeder, M.R., Kranis, H., Skourtsos, E., Andrews, J.E., Henstra, G.A.,
711 Mack, G.H., Muravchik, M., Turner, J.A., Stamatakis, M., 2018. Tectono-sedimentary
712 evolution of the Plio-Pleistocene Corinth rift, Greece. Basin Research 30, 448–479.
713 https://doi.org/10.1111/bre.12260
714 Goldsworthy, M., Jackson, J., Haines, J., 2002. The continuity of active fault systems in
715 Greece. Geophysical Journal International 148, 596–618.
716 https://doi.org/10.1046/j.1365-246X.2002.01609.x
717 Hatzfeld, D., Ziazia, M., Kementzetzidou, D., Hatzidimitriou, P., Panagiotopoulos, D.,
718 Makropoulos, K., Papadimitriou, P., Deschamps, A., 1999. Microseismicity and focal
719 mechanisms at the western termination of the North Anatolian Fault and their
720 implications for continental tectonics. Geophysical Journal International 137, 891–
721 908. https://doi.org/10.1046/j.1365-246x.1999.00851.x
722 IGME, 2006. Geological Map of Greece, 1:50,000 Scale (Pelasgia sheet, 2006; Istaia sheet,
723 1984; Elatia sheet, 1967; Atalanti sheet, 1965).
724 Jackson, Christopher A.-L., Bell, R.E., Rotevatn, A., Tvedt, A.B.M., 2017. Techniques to
725 determine the kinematics of synsedimentary normal faults and implications for fault
726 growth models, in: Childs, C., Holdsworth, R.E., Jackson, C. A.-L., Manzocchi, T.,
727 Walsh, J.J., Yielding, G. (Eds.), The Geometry and Growth of Normal Faults. The
728 Geological Society of London, p. 0. https://doi.org/10.1144/SP439.22

729 Jolivet, L., Faccenna, C., Huet, B., Labrousse, L., Le Pourhiet, L., Lacombe, O., Lecomte, E.,
730 Burov, E., Denèle, Y., Brun, J.-P., Philippon, M., Paul, A., Salaün, G., Karabulut, H.,
731 Piromallo, C., Monié, P., Gueydan, F., Okay, A.I., Oberhänsli, R., Pourteau, A.,
732 Augier, R., Gadenne, L., Driussi, O., 2013. Aegean tectonics: Strain localisation, slab
733 tearing and trench retreat. Tectonophysics, The Aegean: a natural laboratory for
734 tectonics - Neotectonics 597–598, 1–33. https://doi.org/10.1016/j.tecto.2012.06.011
735 Jourdon, A., Le Pourhiet, L., Mouthereau, F., May, D., 2020. Modes of Propagation of
736 Continental Breakup and Associated Oblique Rift Structures. Journal of Geophysical
737 Research: Solid Earth 125, e2020JB019906. https://doi.org/10.1029/2020JB019906
738 Kranis, H., 2007. Neotectonic Basin Evolution in Central-Eastern Mainland Greece: An
739 Overview. Bulletin of the Geological Society of Greece 40, 360–373.
740 https://doi.org/10.12681/bgsg.16621
741 Kranis, H., Palyvos, N., Livaditis, G., Maroukian, H., 2001. The Hyambolis zone:
742 geomorhological and tectonic evidence of a transverse structure in Lokris (Central
743 Greece). Bulletin of the Geological Society of Greece 34, 251–251.
744 https://doi.org/10.12681/bgsg.17020
745 Laó-Dávila, D.A., Al-Salmi, H.S., Abdelsalam, M.G., Atekwana, E.A., 2015. Hierarchical
746 segmentation of the Malawi Rift: The influence of inherited lithospheric heterogeneity
747 and kinematics in the evolution of continental rifts. Tectonics 34, 2399–2417.
748 https://doi.org/10.1002/2015TC003953
749 Lathrop, B.A., Jackson, C. a.-L., Bell, R.E., Rotevatn, A., 2022. Displacement/Length
750 Scaling Relationships for Normal Faults; a Review, Critique, and Revised
751 Compilation. Front. Earth Sci. 10. https://doi.org/10.3389/feart.2022.907543
752 Leeder, M.R., Mack, G.H., Brasier, A.T., Parrish, R.R., McIntosh, W.C., Andrews, J.E.,
753 Duermeijer, C.E., 2008. Late-Pliocene timing of Corinth (Greece) rift-margin fault
754 migration. Earth and Planetary Science Letters 274, 132–141.
755 https://doi.org/10.1016/j.epsl.2008.07.006
756 Lykousis, V., Sakellariou, D., Moretti, I., Kaberi, H., 2007a. Late Quaternary basin evolution
757 of the Gulf of Corinth: Sequence stratigraphy, sedimentation, fault–slip and
758 subsidence rates. Tectonophysics, Deep structure, fault arrays and surface processes
759 within an active graben: The Gulf of Corinth 440, 29–51.
760 https://doi.org/10.1016/j.tecto.2006.11.007
761 Lykousis, V., Sakellariou, D., Moretti, I., Kaberi, H., 2007b. Late Quaternary basin evolution
762 of the Gulf of Corinth: Sequence stratigraphy, sedimentation, fault–slip and
763 subsidence rates. Tectonophysics 440, 29–51.
764 https://doi.org/10.1016/j.tecto.2006.11.007
765 McNeill, L.C., Collier, R.E.Ll., De Martini, P.M., Pantosti, D., D'Addezio, G., 2005. Recent
766 history of the Eastern Eliki Fault, Gulf of Corinth: geomorphology, palaeoseismology
767 and impact on palaeoenvironments. Geophysical Journal International 161, 154–166.
768 https://doi.org/10.1111/j.1365-246X.2005.02559.x
769 McNeill, L.C., Shillington, D.J., Carter, G.D.O., Everest, J.D., Gawthorpe, R.L., Miller, C.,
770 Phillips, M.P., Collier, R.E.Ll., Cvetkoska, A., De Gelder, G., Diz, P., Doan, M.-L.,
771 Ford, M., Geraga, M., Gillespie, J., Hemelsdaël, R., Herrero-Bervera, E., Ismaiel, M.,
772 Janikian, L., Kouli, K., Le Ber, E., Li, S., Maffione, M., Mahoney, C., Machlus, M.L.,
773 Michas, G., Nixon, C.W., Oflaz, S.A., Omale, A.P., Panagiotopoulos, K.,
774 Pechlivanidou, S., Sauer, S., Seguin, J., Sergiou, S., Zakharova, N.V., Green, S.,
775 2019. High-resolution record reveals climate-driven environmental and sedimentary
776 changes in an active rift. Scientific Reports 9, 3116–3116.
777 https://doi.org/10.1038/s41598-019-40022-w
778 Mildon, Z.K., Diercks, M., Roberts, G.P., Faure Walker, J.P., Ganas, A., Papanikolaou, I.,
779 Sakas, V., Robertson, J., Sgambato, C., Mitchell, S., 2024. Transient Aseismic
780 Vertical Deformation Across the Steeply-Dipping Pisia-Skinos Normal Fault (Gulf of

781 Corinth, Greece). Tectonics 43, e2024TC008276-e2024TC008276.
782 https://doi.org/10.1029/2024TC008276
783 Molnar, N.E., Cruden, A.R., Betts, P.G., 2017. Interactions between propagating rotational
784 rifts and linear rheological heterogeneities: Insights from three-dimensional laboratory
785 experiments. Tectonics 36, 420–443. https://doi.org/10.1002/2016TC004447
786 Mouslopoulou, V., Nicol, A., Little, T.A., Walsh, J.J., 2007. Displacement transfer between
787 intersecting regional strike-slip and extensional fault systems. Journal of Structural
788 Geology 29, 100–116. https://doi.org/10.1016/j.jsg.2006.08.002
789 Nixon, C.W., McNeill, L.C., Bull, J.M., Bell, R.E., Gawthorpe, R.L., Henstock, T.J.,
790 Christodoulou, D., Ford, M., Taylor, B., Sakellariou, D., Ferentinos, G.,
791 Papatheodorou, G., Leeder, M.R., Collier, R.E.L.I., Goodliffe, A.M., Sachpazi, M.,
792 Kranis, H., 2016. Rapid spatiotemporal variations in rift structure during development
793 of the Corinth Rift, central Greece. Tectonics 35, 1225–1248.
794 https://doi.org/10.1002/2015TC004026
795 Nixon, C.W., McNeill, L.C., Gawthorpe, R.L., Shillington, D.J., Michas, G., Bell, R.E.,
796 Moyle, A., Ford, M., Zakharova, N.V., Bull, J.M., de Gelder, G., 2024. Increasing
797 fault slip rates within the Corinth Rift, Greece: A rapidly localising active rift fault
798 network. Earth and Planetary Science Letters 636, 118716.
799 https://doi.org/10.1016/j.epsl.2024.118716
800 Palyvos, N., Bantekas, I., Kranis, H., 2006. Transverse fault zones of subtle geomorphic
801 signature in northern Evia island (central Greece extensional province): An
802 introduction to the Quaternary Nileas graben. Geomorphology 76, 363–374.
803 https://doi.org/10.1016/j.geomorph.2005.12.002
804 Pantosti, D., De Martini, P.M., Papanastassiou, D., Lemeille, F., Palyvos, N., Stavrakakis, G.,
805 2004. Paleoseismological Trenching across the Atalanti Fault (Central Greece):
806 Evidence for the Ancestors of the 1894 Earthquake during the Middle Ages and
807 Roman Times. Bulletin of the Seismological Society of America 94, 531–549.
808 https://doi.org/10.1785/0120020207
809 Papanastassiou, D., Cundy, A.B., Gaki-Papanastassiou, K., Frogley, M.R., Tsanakas, K.,
810 Maroukian, H., 2014. The Uplifted Terraces of the Arkitsa Region, NW Evoikos Gulf,
811 Greece: A Result of Combined Tectonic and Volcanic Processes? The Journal of
812 Geology 122, 397–410. https://doi.org/10.1086/676595
813 Papanikolaou, D., 2021. The Geology of Greece. https://doi.org/10.1007/978-3-030-60731-9
814 Papanikolaou, D., Royden, L.H., 2007. Disruption of the Hellenic arc: Late Miocene
815 extensional detachment faults and steep Pliocene-Quaternary normal faults—Or what
816 happened at Corinth? Tectonics 26. https://doi.org/10.1029/2006TC002007
817 Pechlivanidou, S., Cowie, P.A., Hannisdal, B., Whittaker, A.C., Gawthorpe, R.L., Pennos, C.,
818 Riiser, O.S., 2018. Source-to-sink analysis in an active extensional setting: Holocene
819 erosion and deposition in the Sperchios rift, central Greece. Basin Research 30, 522–
820 543. https://doi.org/10.1111/bre.12263
821 Phillips, T.B., Fazlikhani, H., Gawthorpe, R.L., Fossen, H., Jackson, C.A.-L., Bell, R.E.,
822 Faleide, J.I., Rotevatn, A., 2019. The Influence of Structural Inheritance and
823 Multiphase Extension on Rift Development, the NorthernNorth Sea. Tectonics 38,
824 4099–4126. https://doi.org/10.1029/2019TC005756
825 Pirazzoli, P.A., Stiros, S.C., Arnold, M., Laborel, J., Laborel-Deguen, F., 1999. Late holocene
826 coseismic vertical displacements and tsunami deposits near Kynos, Gulf of Euboea,
827 Central Greece. Physics and Chemistry of the Earth, Part A: Solid Earth and Geodesy
828 24, 361–367. https://doi.org/10.1016/S1464-1895(99)00042-3
829 Roberts, G.P., Ganas, A., 2000. Fault-slip directions in central and southern Greece measured
830 from striated and corrugated fault planes: Comparison with focal mechanism and
831 geodetic data. Journal of Geophysical Research: Solid Earth 105, 23443–23462.
832 https://doi.org/10.1029/1999JB900440

833 Roberts, S., Jackson, J., 1991. Active normal faulting in central Greece: an overview.
834 Geological Society, London, Special Publications 56, 125–142.
835 https://doi.org/10.1144/GSL.SP.1991.056.01.09
836 Sakellariou, D., Rousakis, G., Kaberi, H., Kapsimalis, V., Georgiou, P., Kanellopoulos, Th.,
837 Lykousis, V., 2007. Tectono-Sedimentary Structure and Late Quaternary Evolution
838 Of The North Evia Gulf Basin, Central Greece: Preliminary Results. Bulletin of the
839 Geological Society of Greece 40, 451–462. https://doi.org/10.12681/bgsg.16644
840 Saria, E., Calais, E., Stamps, D.S., Delvaux, D., Hartnady, C.J.H., 2014. Present-day
841 kinematics of the East African Rift. Journal of Geophysical Research: Solid Earth
842 119, 3584–3600. https://doi.org/10.1002/2013JB010901
843 Sboras, S., Mouzakiotis, E., Chousianitis, K., Karastathis, V., Evangelidis, C.P., Lazos, I.,
844 Papageorgiou, A., Liakopoulos, S., Iordanidou, K., 2025. Where does the active North
845 Aegean Sea shear stop? Geodynamic and seismotectonic implications from recent
846 strike-slip earthquake occurrences and GPS-based geodetic analysis in Euboea,
847 Phthiotis and Boeotia, Central Greece. Tectonophysics 914, 230917.
848 https://doi.org/10.1016/j.tecto.2025.230917
849 Schmid, T.C., Schreurs, G., Adam, J., 2022. Characteristics of continental rifting in rotational
850 systems: New findings from spatiotemporal high resolution quantified crustal scale
851 analogue models. Tectonophysics 822, 229174.
852 https://doi.org/10.1016/j.tecto.2021.229174
853 Spratt, R.M., Lisiecki, L.E., 2016. A Late Pleistocene sea level stack. Climate of the Past 12,
854 1079–1092. https://doi.org/10.5194/cp-12-1079-2016
855 Vail, P.R., Mitchum, R.M., Jr., Thompson, S., III, 1977. Seismic Stratigraphy and Global
856 Changes of Sea Level, Part 4: Global Cycles of Relative Changes of Sea Level, in:
857 Payton, C.E. (Ed.), Seismic Stratigraphy — Applications to Hydrocarbon Exploration.
858 American Association of Petroleum Geologists, p. 0.
859 https://doi.org/10.1306/M26490C6
860 Van Andel, T H, Perissoratis, C., 2006. Late Quaternary depositional history of the North
861 Evvoikos Gulf, Aegean Sea, Greece. Marine Geology 232, 157–172.
862 https://doi.org/10.1016/j.margeo.2006.07.004
863 Van Andel, T. H., Perissoratis, C., 2006. Late Quaternary depositional history of the North
864 Evvoikos Gulf, Aegean Sea, Greece. Marine Geology 232, 157–172.
865 https://doi.org/10.1016/j.margeo.2006.07.004
866 Walker, R.T., Claisse, S., Telfer, M., Nissen, E., England, P., Bryant, C., Bailey, R., 2010.
867 Preliminary estimate of Holocene slip rate on active normal faults bounding the
868 southern coast of the Gulf of Evia, central Greece. Geosphere 6, 583–593.
869 https://doi.org/10.1130/GES00542.1
870 Wallace, L.M., Beavan, J., McCaffrey, R., Darby, D., 2004. Subduction zone coupling and
871 tectonic block rotations in the North Island, New Zealand. Journal of Geophysical
872 Research: Solid Earth 109. https://doi.org/10.1029/2004JB003241
873 Watkins, S.E., Whittaker, A.C., Bell, R.E., McNeill, L.C., Gawthorpe, R.L., Brooke, S.A.S.,
874 Nixon, C.W., 2018. Are landscapes buffered to high-frequency climate change? A
875 comparison of sediment fluxes and depositional volumes in the Corinth Rift, central
876 Greece, over the past 130 k.y. GSA Bulletin 131, 372–388.
877 https://doi.org/10.1130/B31953.1
878 Wells, D.L., Coppersmith, K.J., 1994. New empirical relationships among magnitude, rupture
879 length, rupture width, rupture area, and surface displacement. Bulletin of the
880 Seismological Society of America 84, 974–1002.
881 https://doi.org/10.1785/BSSA0840040974
882 Whittaker, A.C., Walker, A.S., 2015. Geomorphic constraints on fault throw rates and
883 linkage times: Examples from the Northern Gulf of Evia, Greece. Journal of

884 Geophysical Research: Earth Surface 120, 137–158.
885 https://doi.org/10.1002/2014JF003318
886 Wood, J., Whittaker, A.C., Bell, R.E., Coveney, S.M., Kranis, H.D., 2025. Resolving
887 Coseismic and Aseismic Normal Fault Slip Behaviors From InSAR Time Series of
888 the European Ground Motion Service (EGMS). Tectonics 44, e2025TC008904.
889 https://doi.org/10.1029/2025TC008904
890 Xu, G., Haq, B.U., 2022. Seismic facies analysis: Past, present and future. Earth-Science
891 Reviews 224, 103876. https://doi.org/10.1016/j.earscirev.2021.103876
892 Zwaan, F., Schreurs, G., 2020. Rift segment interaction in orthogonal and rotational
893 extension experiments: Implications for the large-scale development of rift systems.
894 Journal of Structural Geology 140, 104119. https://doi.org/10.1016/j.jsg.2020.104119
895 Zwaan, F., Schreurs, G., Rosenau, M., 2020. Rift propagation in rotational versus orthogonal
896 extension: Insights from 4D analogue models. Journal of Structural Geology 135,
897 103946. https://doi.org/10.1016/j.jsg.2019.103946
898

# Figures & Captions:

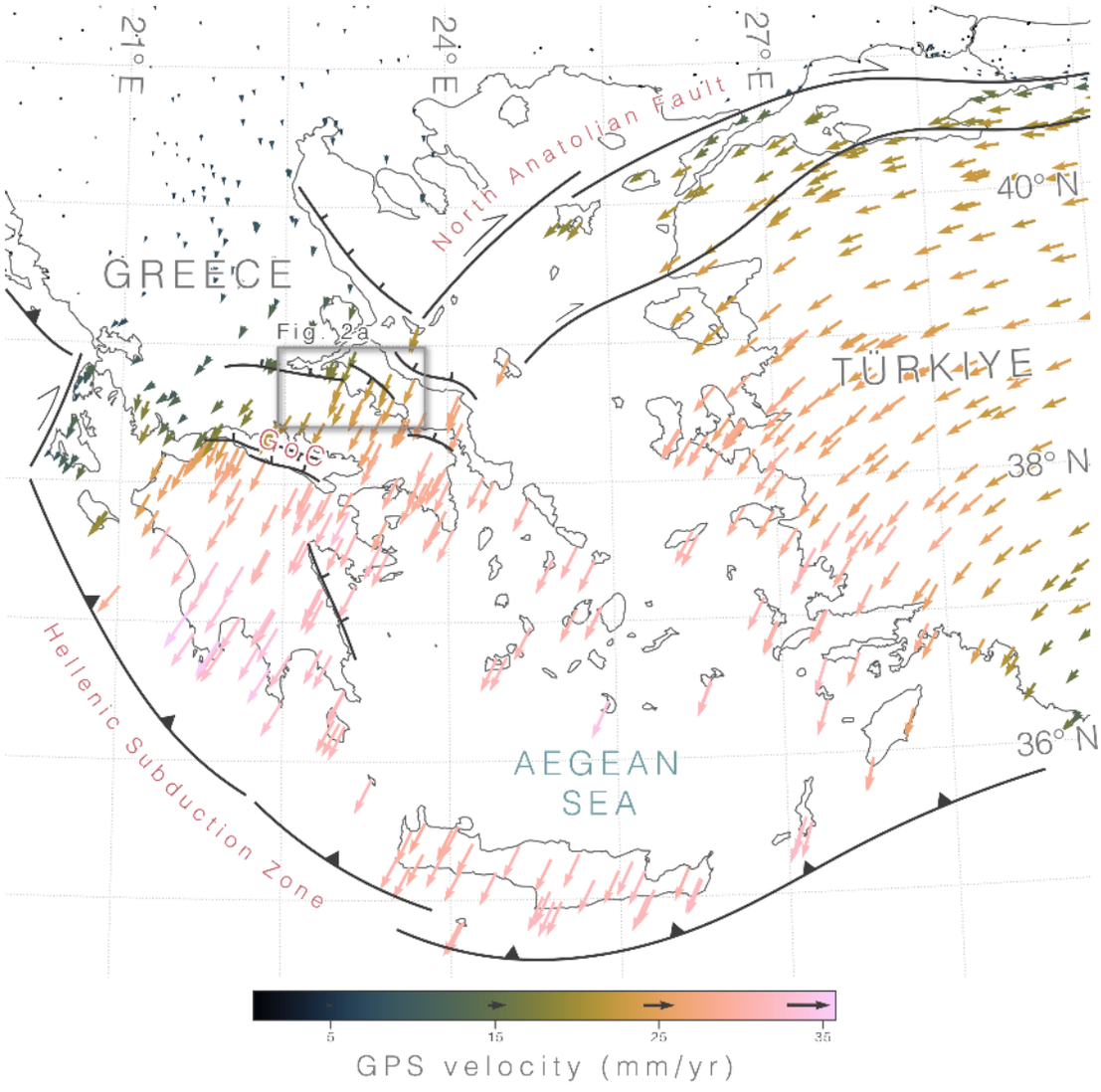


**Figure 1:** Tectonic overview of the Aegean domain with GPS velocity field of the Eastern Mediterranean relative to stable Eurasia from Chousianitis et al. (2024). GoC = Gulf of Corinth. Major fault zones after (Papanikolaou and Royden, 2007).

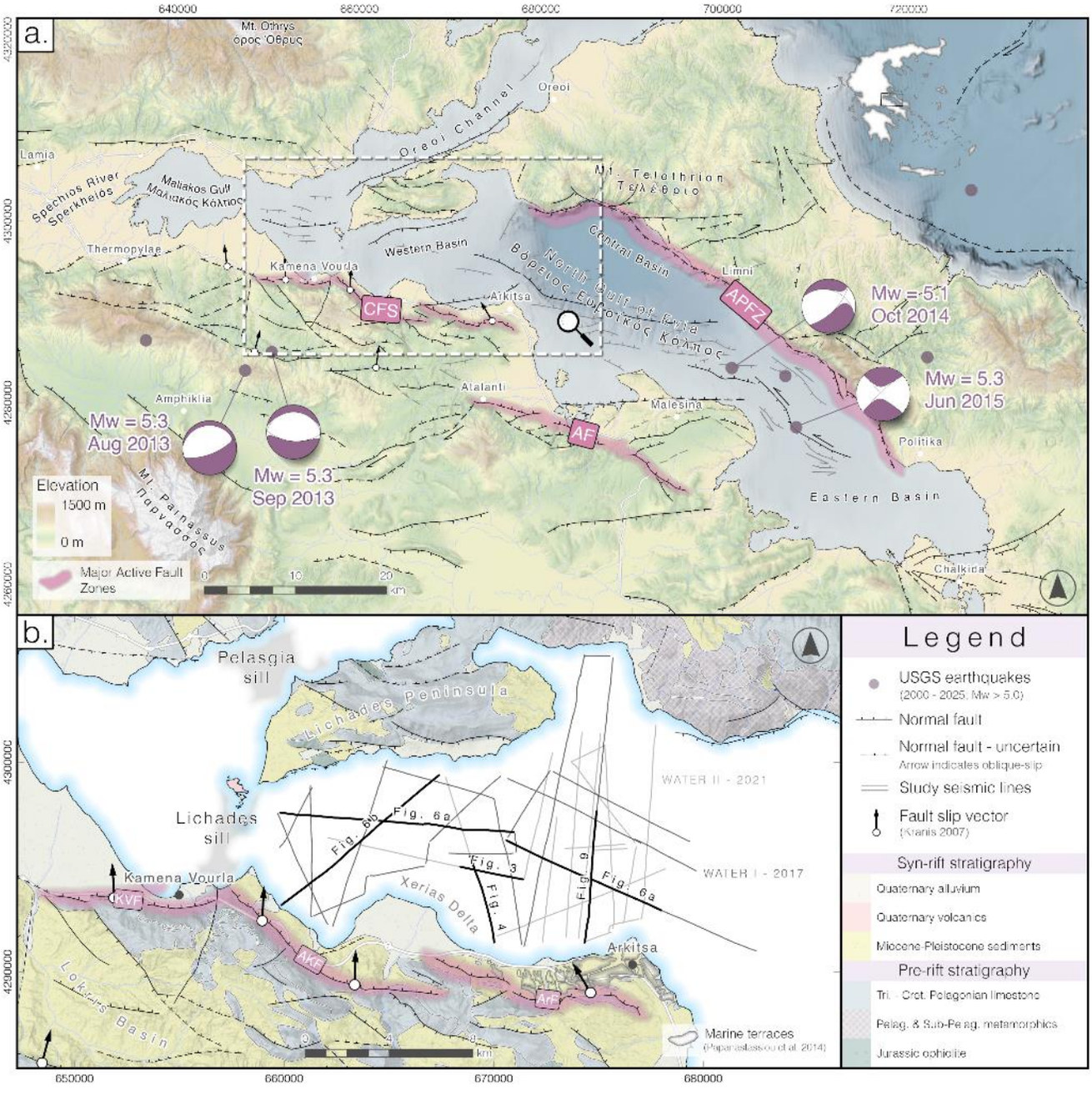


**Figure 2:** a) Regional tectonic map of the North Gulf of Evia, Central Greece. Major active normal fault zones highlighted in purple. Moment tensors of recent Mw > 5 earthquakes from the USGS database (https://earthquake.usgs.gov/earthquakes/search/). CFS = Coastal Fault System, AF = Atalanti Fault, APFZ = Aedipsos-Politika Fault Zone. Onshore fault traces compiled from a number of studies and databases (Galanakis et al., 2025; Ganas et al., 2013; Kranis, 2007) and primary field study. Offshore faults from Caroir et al., (2024). c) Bedrock geology of the Western Basin of the North Gulf of Evia (after IGME, 2006) and offshore seismic reflection data profiles used in this study (see Supplementary Figure S5 for profile

911 numbers). Fault slip vectors after Kranis (2007) and Arkitsa terrace outlines after
912 Papanastassiou et al. (2014). KVF = Kammena Vourla Fault, AKF = Agios Konstantinos
913 Fault, ArF = Arkitsa Fault.

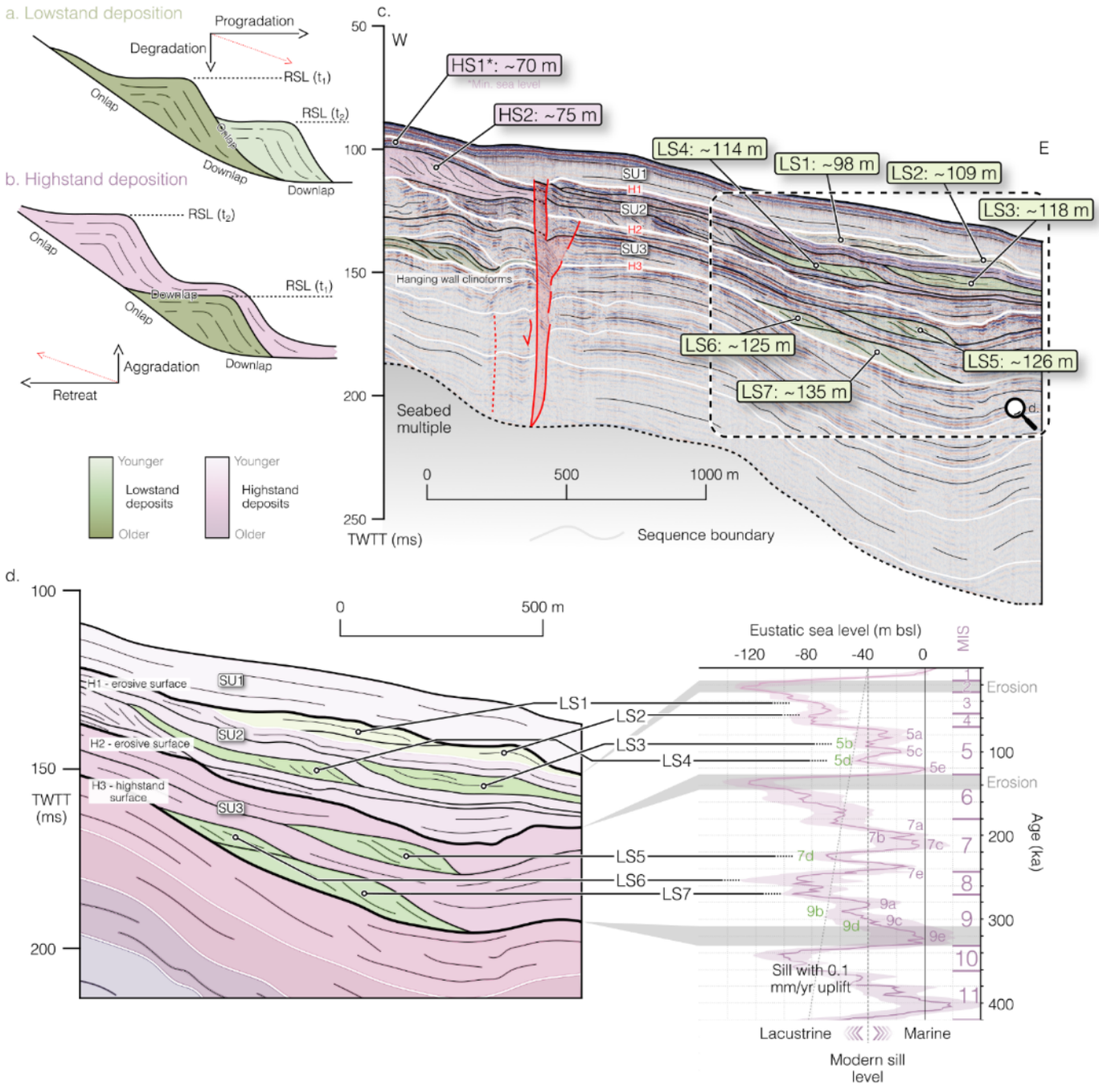


914 **Figure 3:** Schematic cartoons showing clinoform package geometries on a basin slope
915 generated following a fall in relative sea level (RSL) from $t_1$ to $t_2$ to generate lowstand
916 packages (a) and a rise in RSL (b) to generate highstand packages. Modified based on
917 Catuneanu (2002). c. Seismic interpretation of Line 107 (WATER II) showing 7 identified

lowstand packages and 2 marked highstand intervals. Clinoform packages shaded based on highstand or lowstand attribution. Indicated depths are the rollover point of the clinoform package (i.e. base level indicator) based on seismic velocities of 1500 m/s and 1800 m/s for seawater and sediment respectively. Lowstand sequences are only considered for the age model in the footwall of the minor normal fault zone in the west of the seismic line. d. Detailed view of lowstand package interpretation with correlation to eustatic sea level curve of Spratt and Lisiecki (2016). See Supplementary Figure S6 for uninterpreted seismic section.

**Figure 4:** Seismic interpretation of Line 049 (WATER II) with the application of the sequence stratigraphic framework defined in the adjacent line (107) of Figure 3. Marked

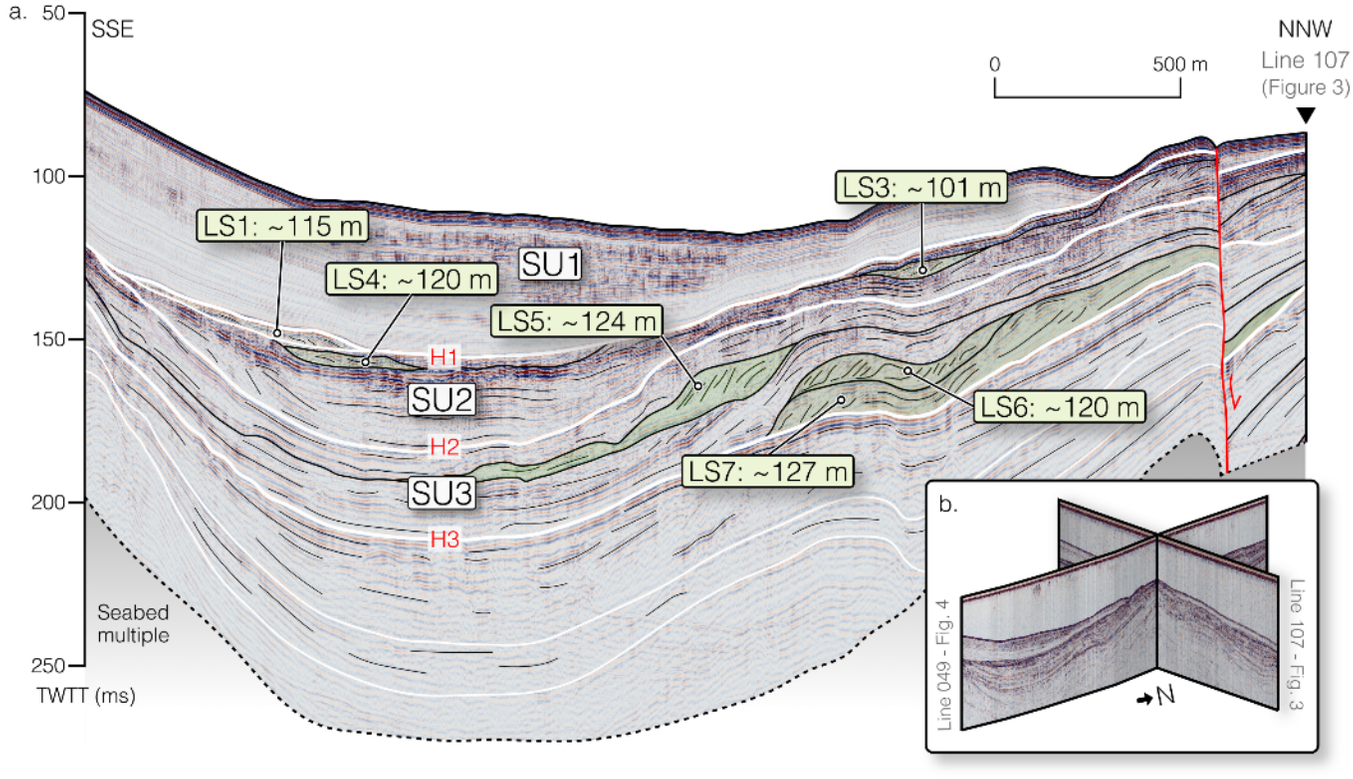


depths correspond to rollover point of clinoform package. b. 3D model showing the geometric interaction between Line 107 (Figure 2) and Line 049 shown in a. See Supplementary Figure S7 for uninterpreted seismic section.

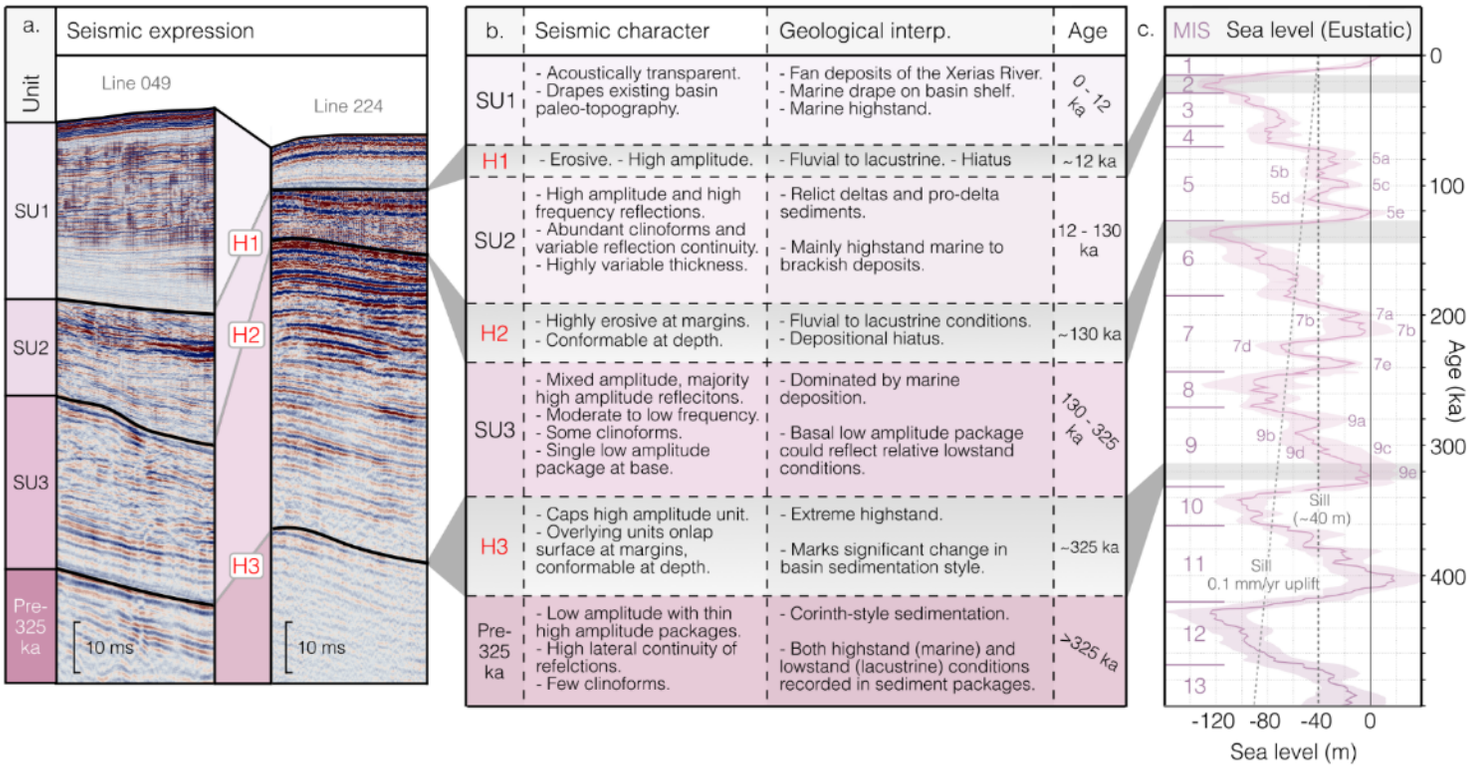


930 **Figure 5:** a. Seismic expression of upper syn-rift stratigraphy including seismic horizons
931 (H1-3) and seismic units (SU1-3). b. Description of seismic character of each unit and
932 horizon, geological interpretation of each unit and horizon and age attributed to each unit and
933 horizon based on correlation to the eustatic sea level curve of Spratt and Lisiecki (2016)
934 shown in c. Further seismic examples of mapped surfaces can be found in Supplementary
935 Figure S2.

936

937

938

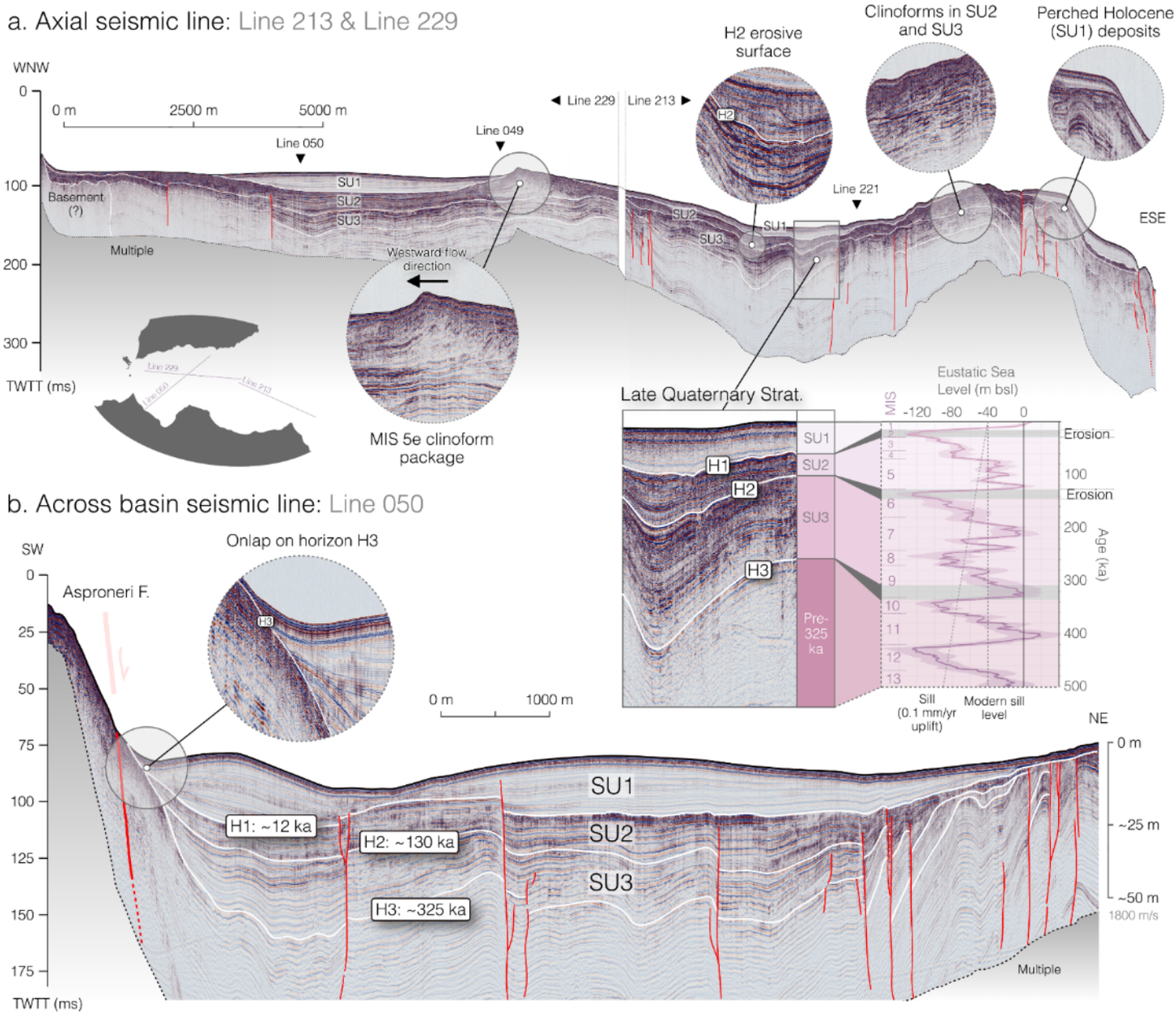


**Figure 6:** a) Axial seismic reflection profile along the Western Basin (Lines 213 and 229) showing typical seismic sedimentary character, clinoform packages, variable Holocene deposit styles, and major depocenter locations. Stratigraphic age correlation (Figure 3) shown as inset with sea level from Spratt and Lisiecki (2016). b) Across-basin seismic reflection profile (Line 050) showing basin structure including Asproneri Fault and high fault density in NE. See Supplementary Figure S8 and S9 for uninterpreted seismic sections.

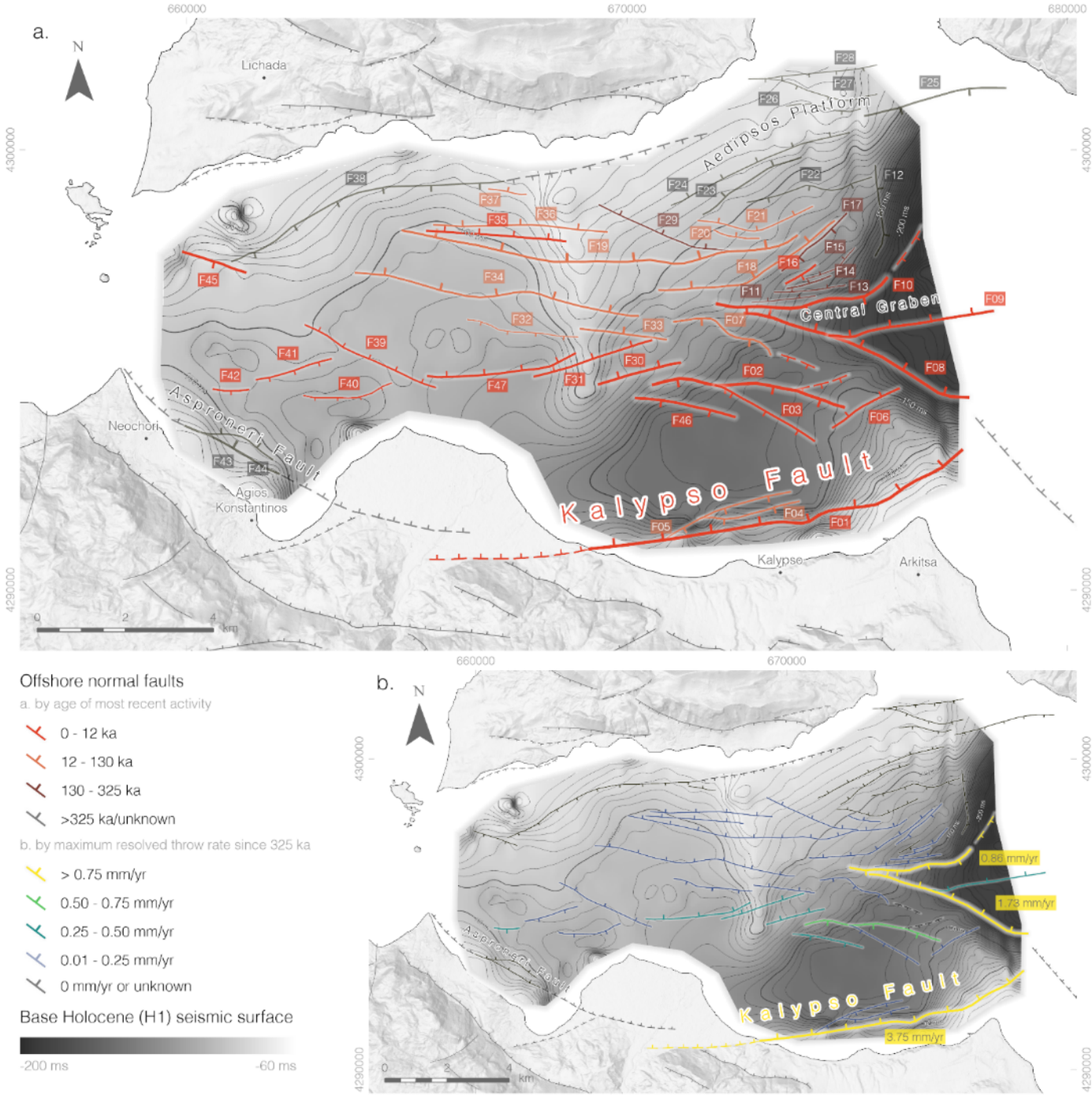


945

946 **Figure 7:** Map of offshore fault network identified in this study on depth to base Holocene
947 (H1), effectively showing pre-Holocene basin geometry (without tectonic or compactional
948 subsidence correction). a) Faults coloured by most recent activity based on offset of youngest
949 key seismic horizon outlined in Figure 6. b) Faults coloured by maximum resolved throw rate
950 over a given interval since ~325 ka (H3) based on throw rates calculated for each key seismic

951 horizon (H1-3). See Supplementary Figure S3 for detail on the generation the H1 surface and
952 Supplementary Table S1 and S2 for further detail on each mapped structure.

953

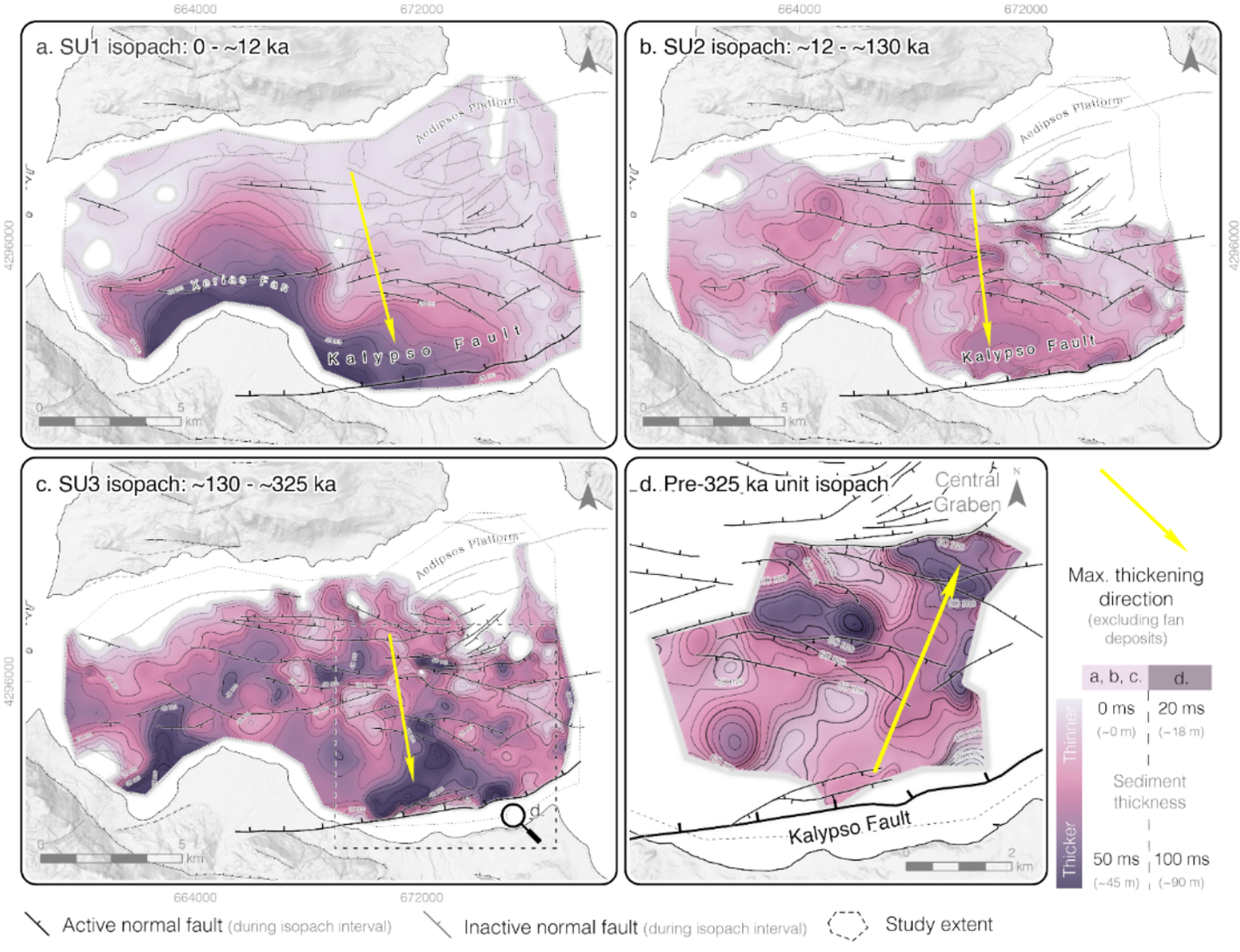


954 **Figure 8:** Isopach maps showing sediment thickness between the three major mapped
955 surfaces in this study (a, b and c) and a package underlying the ~325 ka surface that is only
956 apparent in the southeast of the study area (d). White area within study boundary indicates
957 zero thickness.

958

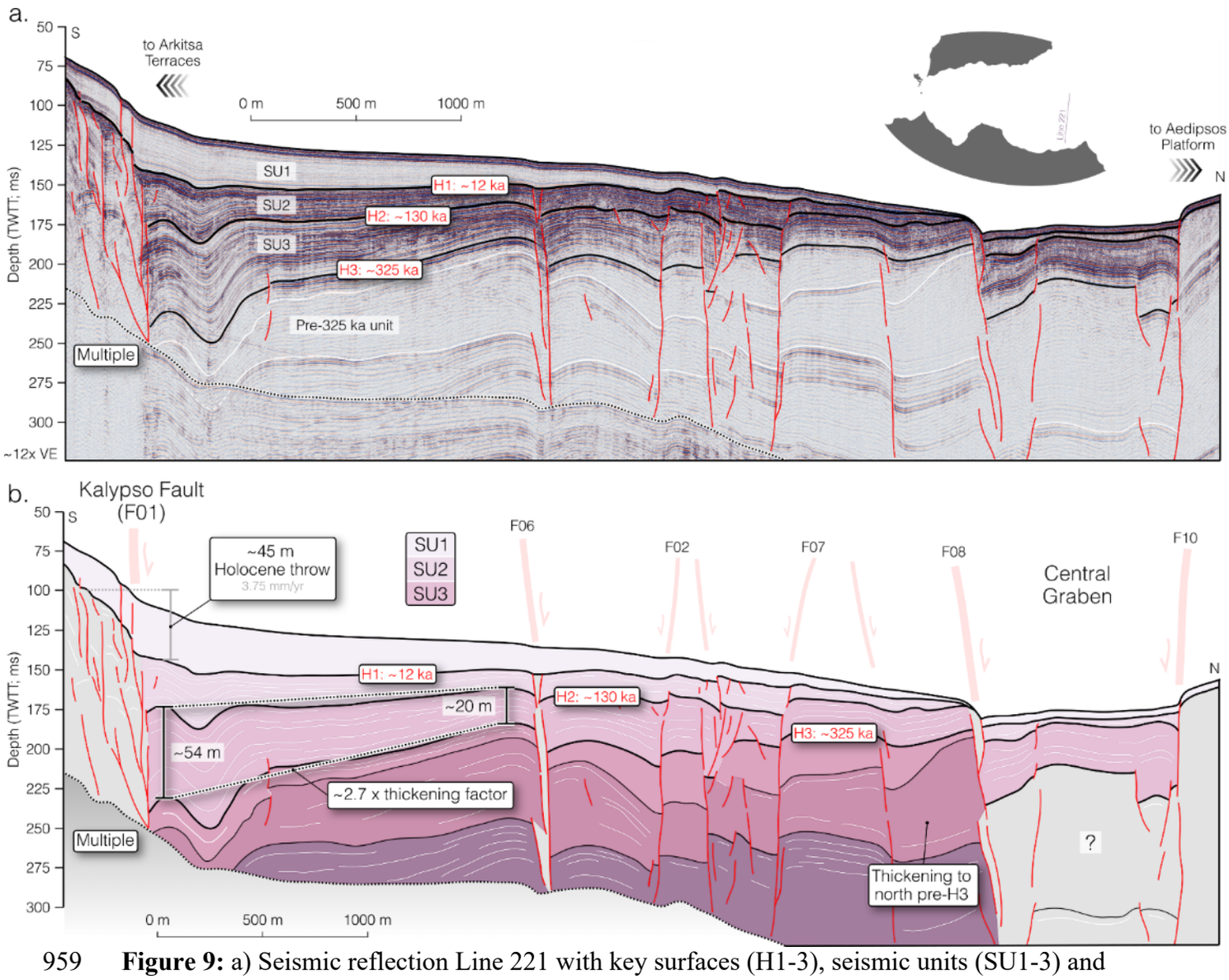


959 **Figure 9:** a) Seismic reflection Line 221 with key surfaces (H1-3), seismic units (SU1-3) and
960 faults shown. b) Interpreted section of line 221. The major Kalypso Fault Zone is shown in
961 the south and active Central Graben in the north. SU1-3 thicken towards the Kalypso Fault
962 (south), older packages with unassigned ages thicken towards the Central Graben (north). See
963 Supplementary Figure S10 for uninterpreted seismic section.

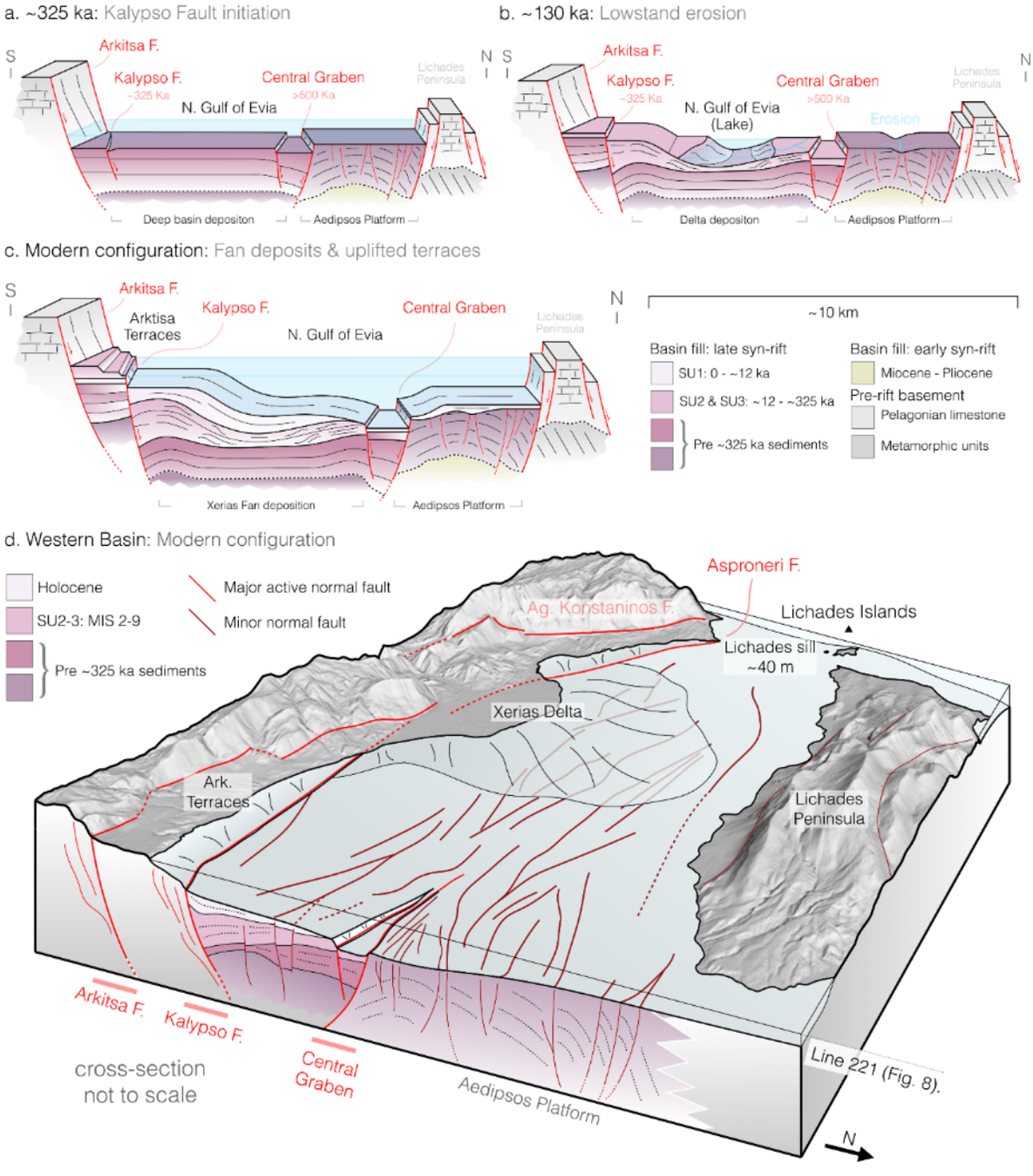


964

965 **Figure 10:** a-c) Schematic evolutionary block models showing structural and sedimentary
966 development of the Western Basin near Arkitsa at ~325 ka (MIS 9e; b), ~130 ka (late-MIS 6;
967 c) and the modern configuration of the basin (d). a) Three-dimensional summary model of the
968 modern Western Basin of the North Gulf of Evia showing fault network, key structures and
969 modern topography. 2x vertical exaggeration. Cross-section not to scale. Looking towards
970 240° at 25° pitch.